Improved Online Optimization-Based Optimal Tracking Control Method for Induction Motor Drives

Rasul Tarvirdilu-Asl, *Student Member, IEEE*, Shamsuddeen Nalakath, *Senior Member, IEEE*, Zekun Xia, *Student Member, IEEE*, Yingguang Sun, *Member, IEEE*, Jason Wiseman, and Ali Emadi, *Fellow, IEEE*

***Abstract*—An online optimization-based optimal tracking control method to control IM drives in the entire speed and torque ranges is proposed in this article. The main feature of the proposed method is considering the nonlinear core saturation effects in generating the optimal reference currents in MTPA, field-weakening, and maximum torque per voltage (MTPV) regions. Constrained optimization problems are formulated and solved using Lagrange multipliers method to derive improved nonlinear MTPA and MTPV optimality conditions. Unlike most of the existing loss minimization methods in the literature, using optimal reference point look-up tables is avoided in the proposed method. Moreover, the effects of stator resistive drops, dc-link voltage variations, and inverter nonlinear voltage drop, which are usually neglected in the literature, are considered in generating optimal reference currents. A new straightforward and well-structured optimal reference point calculation scheme is proposed by dividing the operating plane of IM into four regions. The optimal reference currents in each region are then generated by solving the corresponding optimization problem. The smooth operation and transition of the proposed control method between MTPA and field-weakening regions are verified using simulations. The effectiveness of the proposed method is experimentally validated on a 4.7-kW, 4-pole, three-phase induction motor drive.**

***Index Terms*—Field oriented control, field weakening, induction motor drives, loss minimization, magnetic saturation, optimal control, torque control, traction motors, variable speed drives.**

I. Introduction

INDUCTION motors (IMs) are the widely used electric motors in the industry [1] owing to their robustness, simple technology, lower manufacturing and maintenance cost, and high reliability [2], [3]. Significant researches have been contributed in developing novel control methods for IM drives to fulfill the industrial requirements for highly efficient adjustable speed drives to operate over wide speed and torque ranges. The tendency to reduce the use of rare-earth materials especially in the automotive sector due to their high cost and limited supply chain has been another reason for this growing research on developing advanced control methods for IM drives [3], [4]. The efficiency optimization methods are generally classified into two broad categories: search methods and model-based methods [5], [6]. The former requires iterative process to adjust the optimal operating point by changing the reference flux magnitude. An online method based on repetitive measurement of the input power is proposed in [7] to optimize the efficiency of IM drives. This method has a slow convergence rate and it introduces extra undesirable speed and torque ripples [8]. The latter is fast and simple and inherently suitable for vector control methods, but it is highly dependent on the accuracy of the machine parameters [3]. The parameter variations at different operating conditions can lead to nonoptimal operating point selection. The implemented loss minimization control methods can be either scalar or vector control. In the scalar control, optimum air gap flux is adjusted to achieve minimum loss condition. On the other hand, in the vector control, optimal d- and q-axis stator current vectors (i_{ds}, i_{qs}) to satisfy minimal loss condition are calculated and applied. Better power factor control and fast dynamic response are the benefits of the vector control approach [9]. Direct torque control [10]–[12] and field-oriented control (FOC) [13], [14] are the two commonly used methods in adjustable speed IM drives [15], [16]. Several other control methods including scalar *v/f* control [17]–[20], model predictive control [15], [16], [21], and neural-network-based control [22], [23] are also employed in IM drives. Selection of the appropriate control scheme is highly dependent on the application requirements for the drive.

A model-based maximum torque per power losses algorithm is proposed in [2] for the indirect field-oriented control of IM drives in constant torque region. Optimal reference points are found by minimizing total losses of IM including copper and core losses using the Lagrange method. A maximum torque per ampere (MTPA) method for low-speed torque control of traction IM drives is proposed in [4]. The optimization problem is solved offline considering magnetic saturation effects and a look-up table (LUT) of optimal flux for a given torque command in the experimental implementation of the proposed method. In [8], an offline LUT-based optimization problem is solved to calculate the optimal reference flux to minimize system-level losses in

Manuscript received September 23, 2019; revised December 6, 2019 and February 3, 2020; accepted February 16, 2020. Date of publication February 24, 2020; date of current version June 23, 2020. This work was supported in part by the NSERC/OCE TargetGHG Collaborative Research and Development Program under Project No. 27904 with BorgWarner Waterloo Inc. Recommended for publication by Associate Editor Y. Yang. *(Corresponding author: Rasul Tarvirdilu-Asl.)*

Rasul Tarvirdilu-Asl, Shamsuddeen Nalakath, Zekun Xia, and Ali Emadi are with the McMaster Automotive Resource Center, McMaster University, Hamilton, ON L8S 4L8, Canada (e-mail: tarvirdr@mcmaster.ca; nalakas@mcmaster.ca; xiaz9@mcmaster.ca; emadi@mcmaster.ca).

Yingguang Sun and Jason Wiseman are with the BorgWarner Inc., Waterloo Technical Center, Kitchener, ON N2G 4X8, Canada (e-mail: yisun@borgwarner.com; jwiseman@borgwarner.com).

Color versions of one or more of the figures in this article are available online at http://ieeexplore.ieee.org.

Digital Object Identifier 10.1109/TPEL.2020.2976037

IM drives in both low-speed and field-weakening regions while neglecting the magnetic nonlinearities. In [5], approximate suboptimal solutions to minimize copper losses of IM drives in constant torque region by neglecting transient state losses are calculated offline. The method is verified by LUT-based experimental implementation. An offline model-based loss minimization by neglecting magnetic saturation for low-speed torque control of IM is proposed in [9]. The optimal points are stored in LUTs to incorporate in experimental testing of the proposed method. In [3], optimal reference flux is calculated offline to minimize IM losses for a given torque demand and reference speed using a proposed maximum efficiency per torque (MEPT) algorithm. Comparing experimental efficiency calculation results of MEPT and MTPA reveals their quite similar performance in machines with higher Joule losses. Several other loss minimization algorithms are proposed in [6], [24]–[31]. A comparison of real-time loss minimization techniques in the literature is given in [1]. Most of the existing methods in the literature are offline and LUT-based. Moreover, the magnetic saturation effect is usually neglected in generating optimal operating points. The maximum torque production capability of IM cannot be achieved if the saturation effect is neglected [32]. Optimal operating points in the field weakening region are determined considering both stator current amplitude and dc-link voltage constraints. An MTPA control of IM drives in the field-weakening region is proposed in [33]. The performance of four field weakening control schemes for IM drives is compared in [34] in terms of complexity, computational burden, and robustness. Improving the field-weakening operation of IM drives has been investigated in many other works in the literature [6], [35]–[46]. However, magnetic saturation, stator resistive voltage drop, and inverter nonlinear voltage drop are usually ignored in most of the studies leading to a nonoptimal point selection.

The key contribution of this article is an optimization-based online optimal tracking control method for wide-speed and torque range control of IM drives considering magnetic core saturation effects. The magnetic core saturation effects, which are usually ignored in the literature, are considered in calculation of the optimal reference currents. The optimization problems are formulated and solved using Lagrange method to derive improved analytical equations for nonlinear MTPA and maximum torque per voltage (MTPV) optimality conditions. A simple and straightforward online optimal tracking control algorithm is proposed by dividing the entire torque-speed plane into four regions to control IM in MTPA, field-weakening, and MTPV regions. The effect of IM resistive voltage drops, inverter nonlinear voltage drop, and dc-link voltage variations, which are usually neglected in the literature, are all considered in calculating the optimal reference points. The effectiveness and smooth operation of the proposed method is experimentally validated on a 4.7-kW, 4-pole, three-phase IM drive.

The article is organized as follows. In Section II, the fundamentals of decoupled torque and flux control of IM under FOC condition are given. The proposed nonlinear MTPA and MTPV optimality conditions are presented in Section III. The equations for field-weakening control and nonlinear inverter voltage drop compensation are also given in the same section. In Section IV, the flowchart of the proposed online optimal tracking in the entire torque and speed ranges is presented. The performance of the proposed method is validated using experimental results in Section V. Finally, the article is concluded in Section VI.

II. Fundamentals of Field-Oriented Control of IM

The stator and rotor voltage equations of a squirrel-cage IM in a synchronously rotating reference *d–q* frame are

$$\begin{cases} v_{\rm ds} = R_s i_{\rm ds} + \dfrac{d\lambda_{\rm ds}}{dt} - \omega\lambda_{\rm qs} \\ v_{\rm qs} = R_s i_{\rm qs} + \dfrac{d\lambda_{\rm qs}}{dt} + \omega\lambda_{\rm ds} \\ 0 = v_{\rm dr} = R_r i_{\rm dr} + \dfrac{d\lambda_{\rm dr}}{dt} - (\omega - \omega_{\rm me})\,\lambda_{\rm qr} \\ 0 = v_{\rm qr} = R_r i_{\rm qr} + \dfrac{d\lambda_{\rm qr}}{dt} + (\omega - \omega_{\rm me})\,\lambda_{\rm dr} \end{cases} \tag{1}$$

where *v*, *i*, λ, *R*, ω, and $\omega_{\rm me}$ stand for voltage, current, flux linkage, resistance, synchronous speed, and rotor speed, respectively. The equations for stator and rotor are denoted by subscripts "s" and "r," respectively. The flux linkage terms in (1) can be calculated using

$$\begin{cases} \lambda_{\rm ds} = L_s i_{\rm ds} + L_m i_{\rm dr} \\ \lambda_{\rm qs} = L_s i_{\rm qs} + L_m i_{\rm qr} \\ \lambda_{\rm dr} = L_r i_{\rm dr} + L_m i_{\rm ds} \\ \lambda_{\rm qr} = L_r i_{\rm qr} + L_m i_{\rm qs} \end{cases} \tag{2}$$

where L_m, L_s, and L_r represent magnetizing (mutual) inductance, stator inductance, and rotor inductance, respectively. Stator and rotor inductances can be found by adding the corresponding leakage inductance term to the magnetizing inductance as

$$\begin{cases} L_s = L_m + L_{\rm ls} \\ L_r = L_m + L_{\rm lr} \end{cases} \tag{3}$$

where $L_{\rm ls}$ and $L_{\rm lr}$ stand for leakage inductances of stator and rotor, respectively.

Achieving decoupled control over flux and torque is the main aim in FOC. By aligning rotor field with *d*-axis ($\lambda = \lambda_{\rm dr}$, $\lambda_{\rm qr} = 0$), rotor flux can be independently controlled by controlling $i_{\rm ds}$ as

$$\lambda_r = \lambda_{\rm dr} = L_m i_{\rm ds}. \tag{4}$$

Note that assuming ($\lambda_{\rm qr} = 0$) results in ($i_{\rm dr} = 0$) under steady-state condition based on rotor *d*-axis voltage equation in (1). Shaft torque can then be controlled by controlling $i_{\rm qs}$ as

$$T = \frac{3pL_m}{4L_r} L_m i_{\rm ds} i_{\rm qs} = k L_m i_{\rm ds} i_{\rm qs} \tag{5}$$

where *p* is the number of poles. Therefore, flux and torque can be independently controlled under FOC by controlling $i_{\rm ds}$ and $i_{\rm qs}$ using both (4) and (5). Selection of an optimal pair of ($i_{\rm ds}$, $i_{\rm qs}$) for a specific operating point determined by reference speed and reference torque is the main purpose in optimal tracking control.

TABLE I
IM SPECIFICATIONS AND PARAMETERS

Variable	Value
Number of poles (p)	4
DC-link voltage (V_{DC})	55 V
Rated power	4.7 kW
Rated torque	9 Nm
Rated current	80.5 A
Rated i_{ds}	90 A
Rated speed	5000 r/min
Maximum power	15 kW for 1 min at speeds up to 2200 rpm
Maximum torque	70 Nm at 400 A (phase current)
Maximum speed	5000 r/min
Stator resistance (R_s) at 25°C	2.5 mΩ
Rotor resistance (R_r)	1.45 mΩ
Stator leakage inductance (L_{ls})	0.0114 mH
Rotor leakage inductance (L_{lr})	0.0114 mH

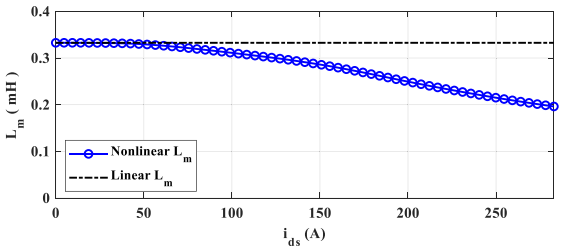

Fig. 1. Measured nonlinear magnetizing inductance of the test IM.

In determination of optimal operating points, both stator current and dc-link voltage constraints have to be considered as

$$\begin{cases} i_{\rm ds}^2 + i_{\rm qs}^2 \le I_{\rm max}^2 \\ v_{\rm ds}^2 + v_{\rm qs}^2 \le V_{\rm max}^2 \end{cases} \tag{6}$$

where $I_{\rm max}$ and $V_{\rm max}$ stand for maximum phase current and maximum attainable phase voltage of IM, respectively. The former is determined based on thermal constraints and the latter is calculated considering both dc-link voltage limitations and the implemented modulation scheme.

A 4.7-kW, 4-pole, three-phase IM is used as the test machine in this study. The motor is characterized using conventional locked-rotor and no-load tests. The parameters and specifications of the test IM are given in Table I. The measured nonlinear magnetizing inductance is presented in Fig. 1. Interpolation is used to estimate the value of the magnetization inductance between two measured data points. The linear (nominal) magnetizing inductance is also shown in this figure. Note that stator and rotor leakage inductances ($L_{\rm ls}$ and $L_{\rm lr}$) are assumed to be constant. Nonlinear $i_{\rm ds}$–$i_{\rm qs}$ plane of the test IM is given in Fig. 2. The red circle is the maximum current limit of IM. Voltage limit ellipses for three different synchronous speeds (2776, 5200, and 14995 rpm) are also given. It can be observed that as the speed increases the feasible operating region is narrowed. As flux is regulated using $i_{\rm ds}$, a minimum $i_{\rm ds}$ limit of $I_{\rm ds,min} = 15$ A (shown in Fig. 2) is considered to maintain a minimum flux under all operating conditions. Based on Fig. 1, the saturation limit for the magnetization inductance can be estimated to be around $I_{\rm ds,sat} = 150$ A (shown in Fig. 2). The saturation limit needs to

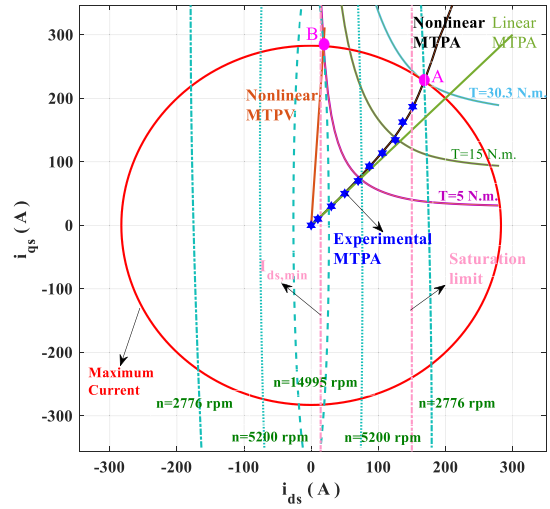

Fig. 2. Nonlinear $i_{\rm ds}$–$i_{\rm qs}$ trajectory of the test IM.

be considered to avoid overexcitation. The experimental MTPA which is found by manually searching the maximum torque for a constant magnitude of stator current is also shown in Fig. 2 for comparison. It shows the nonlinear MTPA closely match with the experimental MTPA.

III. PROPOSED NONLINEAR MTPA AND MTPV CONDITIONS

An optimization-based method is proposed in this article to derive the optimal operating conditions of IM in MTPA, field-weakening, and MTPV regions considering nonlinear magnetic saturation effects.

A. Proposed Nonlinear MTPA Condition

To determine nonlinear MTPA criteria, the minimization problem is formulated as

$$\begin{cases} \text{minimize}_{i_{\rm ds},\, i_{\rm qs}} & i_{\rm ds}^2 + i_{\rm qs}^2 \\ \text{s.t.} & T_{\rm ref} = kL_m i_{\rm ds} i_{\rm qs}. \end{cases} \tag{7}$$

The minimization problem is solved using Lagrange multipliers method. The Lagrange function is constructed as

$$\mathcal{L}\left(i_{\rm ds}, i_{\rm qs}, \lambda\right) = -i_{\rm ds}^2 - i_{\rm qs}^2 + \lambda\left(kL_m i_{\rm ds} i_{\rm qs} - T_{\rm ref}\right) \tag{8}$$

where λ is the Lagrange coefficient. The minimization problem is solved as

$$\begin{cases} \dfrac{\partial \mathcal{L}}{\partial i_{\rm ds}} = 0 \\ \dfrac{\partial \mathcal{L}}{\partial i_{\rm qs}} = 0 \\ \dfrac{\partial \mathcal{L}}{\partial \lambda} = 0 \end{cases} \rightarrow \begin{cases} \lambda = \dfrac{2i_{\rm ds}}{ki_{\rm qs}\left(L_m + \dot{L}_m i_{\rm ds}\right)} \\ \lambda = \dfrac{2i_{\rm qs}}{kL_m i_{\rm ds}} \\ T_{\rm ref} = kL_m i_{\rm ds} i_{\rm qs} \end{cases}$$

$$\rightarrow \begin{cases} i_{\rm qs} = i_{\rm ds}\sqrt{\dfrac{1}{1 + \dfrac{\dot{L}_m}{L_m} i_{\rm ds}}} \\ T_{\rm ref} = kL_m i_{\rm ds} i_{\rm qs}. \end{cases} \tag{9}$$

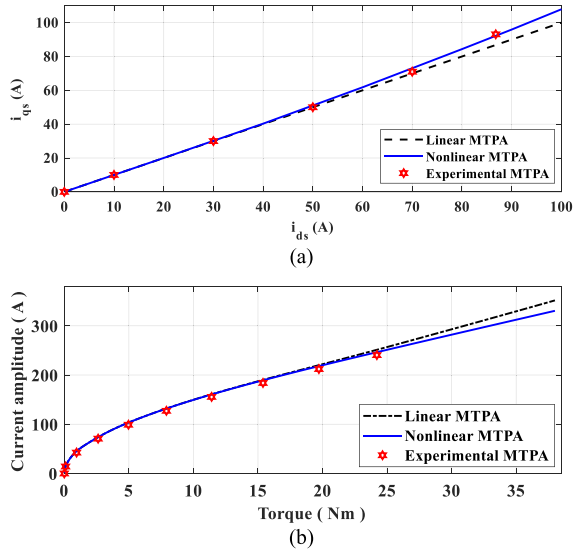

Fig. 3. Linear, nonlinear, and experimental MTPA points. (a) Magnified view of $i_{\rm ds}$–$i_{\rm qs}$ plane. (b) Stator current amplitude versus reference torque under linear and nonlinear MTPA conditions.

Note that $\dot{L}_m$ represents the first derivative of the magnetizing inductance with respect to $i_{\rm ds}$ which is calculated using

$$\dot{L}_m = \frac{dL_m}{di_{\rm ds}} = \frac{L_m\left(i_{\rm ds}+\Delta\right) - L_m\left(i_{\rm ds}-\Delta\right)}{2\Delta} \tag{10}$$

where Δ is a constant small current step. In this article,L_m is from LUT and $\Delta = 0.01$ A. Finally, solving the following nonlinear equation gives the proposed optimal operating point in MTPA region.

$$\left(T_{\rm ref} - kL_m i_{\rm ds}^2 \sqrt{\frac{1}{1+\frac{\dot{L}_m}{L_m} i_{\rm ds}}}\right)^2 = 0. \tag{11}$$

If the saturation effect is neglected, $\dot{L}_m = 0$, and (11) is simplified to the well-known linear MTPA condition for IM in the literature [4], [6] as

$$i_{\rm qs} = i_{\rm ds}. \tag{12}$$

Both linear and the proposed nonlinear MTPA curves are shown on $i_{\rm ds}$–$i_{\rm qs}$ trajectory of IM in Fig. 2. It can be seen that the nonlinear curve diverges from the linear curve as $i_{\rm ds}$ increases. The magnified view of both linear and nonlinear MTPA curves in the region where $i_{\rm ds} < 100$ A is shown in Fig. 3(a). It can be observed that nonlinear MTPA curve diverges from linear curve after around $i_{\rm ds} = 50$ A. This point is where nonlinear magnetizing inductance diverges from the linear (nominal) inductance, as shown in Fig. 1. To show the nonlinear curve is a better MTPA as compared to linear curve, the stator current amplitude is plotted for different torque levels in Fig. 3(b). It can be seen that the current amplitude is lower with the proposed nonlinear MTPA for a similar load torque and hence better MTPA criteria. The difference gets more considerable as the load torque increases where IM operates in the saturation region. Hence, neglecting the magnetic saturation effect leads to a nonoptimal operating point selection in MTPA region which reduces the efficiency. Moreover, based on Fig. 2, the maximum attainable torque (30.3 Nm) with nonlinear MTPA under the current limit is bigger than the maximum achievable torque (28.8 Nm) with linear MTPA.

Both experimental and analytically calculated MTPA points using the proposed algorithm are plotted on the $i_{\rm ds}$–$i_{\rm qs}$ trajectory in Figs. 2 and 3(a). It can be seen that analytical results are in a very good coincidence with experimentally obtained MTPA data. The measured torques for different current amplitudes are plotted in Fig. 3(b). It can be observed that experimentally obtained torque values are in good agreement with analytically calculated nonlinear MTPA points.

B. Proposed Nonlinear MTPV Condition

The optimization problem to calculate the optimal reference points in the very high-speed region (MTPV region) is formulated as

$$\begin{cases} \text{minimize}_{i_{\rm ds},i_{\rm qs}} & v_{\rm ds}^2 + v_{\rm qs}^2 = \left(\omega\sigma L_s i_{\rm qs}\right)^2 + \left(\omega L_s i_{\rm ds}\right)^2 \\ \text{s.t.} & T_{\rm ref} = kL_m i_{\rm ds} i_{\rm qs} \end{cases} \tag{13}$$

where σ is the leakage factor of IM defined as

$$\sigma = 1 - \frac{L_m^2}{L_r L_s}. \tag{14}$$

As the speed is very high in the MTPV region, the stator resistive drop terms are negligible compared to the speed-dependent terms. Hence, resistive drop terms are neglected in voltage equations to simplify the analysis. To simplify the expressions, the nonlinear term $L_s\sigma$ is replaced with ζ in (13). ζ is a nonlinear function of $i_{\rm ds}$. Similar to the minimization problem in MTPA region, Lagrange function is constructed as

$$\begin{aligned} \mathcal{L}\left(i_{\rm ds}, i_{\rm qs}, \lambda\right) = & -\left(\omega\zeta i_{\rm qs}\right)^2 - \left(\omega L_s i_{\rm ds}\right)^2 \\ & + \lambda\left(kL_m i_{\rm ds} i_{\rm qs} - T_{\rm ref}\right). \end{aligned} \tag{15}$$

Solving the minimization problem using Lagrange multipliers method results in the proposed nonlinear equation for MTPV region as

$$\begin{aligned} & \frac{\zeta\dot{\zeta}T_{\rm ref}^2}{k^2L_m^2 i_{\rm ds}^2} + L_s^2 i_{\rm ds} + L_s\dot{L}_s i_{\rm ds}^2 \\ & \quad - \frac{\zeta^2 T_{\rm ref}^2}{k^2 L_m^3 i_{\rm ds}^3}\left(\dot{L}_m i_{\rm ds} + L_m\right) = 0. \end{aligned} \tag{16}$$

The difference between both L_s and L_r with L_m is a constant leakage inductance, hence, $\dot{L}_m = \dot{L}_s = \dot{L}_r$. Moreover, $\dot{\zeta}$ can be calculated using

$$\dot{\zeta} = \dot{L}_s - \frac{2L_m\dot{L}_m L_r - L_m^2\dot{L}_r}{L_r^2}. \tag{17}$$

If the nonlinear saturation effect is neglected $\dot{L}_m = \dot{\zeta} = 0$, and the widely used linear MTPV equation for IM drives [6], [41], [44] is obtained as

$$i_{\rm qs} = \frac{L_s}{\zeta} i_{\rm ds} = \frac{1}{\sigma} i_{\rm ds}. \tag{18}$$

The nonlinear MTPV curve is shown in Fig. 2. To analyze the effects of neglecting core saturation, both linear and nonlinear

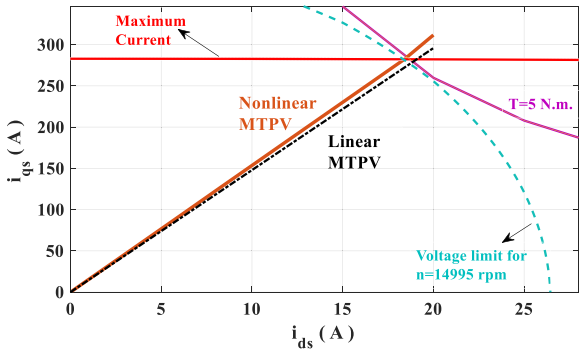

Fig. 4. Linear and nonlinear MTPV curves.

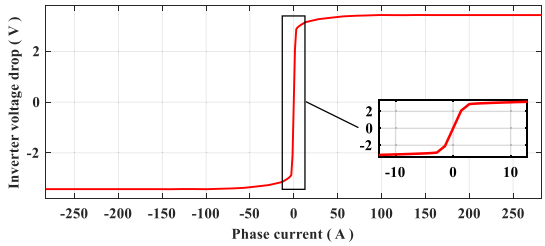

Fig. 5. Measured inverter nonlinear voltage drop.

MTPV curves are plotted in Fig. 4. As $i_{\rm ds}$ (flux) is small under MTPV condition, IM operates in the linear region of the magnetization curve. Hence, the difference between linear and nonlinear MTPV curves is not significant.

C. Operating Point in the Field-Weakening Region

The allowable operating area inside the voltage ellipses shrinks as the speed increases if the available dc-link voltage is limited. Hence, voltage constraint is the main limiting factor in determining the optimal reference points in the field-weakening region. The operating points diverge from the MTPA curve in the field-weakening region by reducing $i_{\rm ds}$ to keep the reference points on the voltage curve. If the reference torque is smaller than the maximum achievable torque by IM, the optimal operating points will be the intersection point of the reference torque curve and the voltage curve as

$$\begin{cases} v_{\rm ds}^2 + v_{\rm qs}^2 = V_{\rm max}^2 \\ T_{\rm ref} = kL_m i_{\rm ds} i_{\rm qs} \end{cases} \rightarrow \begin{cases} \left(R_s i_{\rm ds} - \omega\lambda_{\rm qs}\right)^2 + \left(R_s i_{\rm qs} + \omega\lambda_{\rm ds}\right)^2 = V_{\rm max}^2 \\ T_{\rm ref} = kL_m i_{\rm ds} i_{\rm qs} \end{cases} \tag{19}$$

where $V_{\rm max}$ is the maximum attainable phase-voltage amplitude. If the inverter voltage drop is neglected, $V_{\rm max}$ should be $V_{\rm dc}/\sqrt{3}$ considering the SVPWM modulation scheme implemented in the test setup.

Further increasing the speed in the field-weakening region will result in hitting the current limit under a specific reference torque. The shaft torque can no longer track the reference torque after the current reaches the limit. On the other hand, if the reference torque is bigger than the maximum achievable torque of IM, by increasing the speed, the optimal reference points will move from the MTPA curve (point A in Fig. 2) toward the intersection of the voltage curve and the maximum current limit curve as

$$\begin{cases} v_{\rm ds}^2 + v_{\rm qs}^2 = V_{\rm max}^2 \\ i_{\rm ds}^2 + i_{\rm qs}^2 = I_{\rm max}^2 \end{cases} \rightarrow \begin{cases} \left(R_s i_{\rm ds} - \omega\lambda_{\rm qs}\right)^2 + \left(R_s i_{\rm qs} + \omega\lambda_{\rm ds}\right)^2 = V_{\rm max}^2 \\ i_{\rm ds}^2 + i_{\rm qs}^2 = I_{\rm max}^2. \end{cases} \tag{20}$$

Note that stator resistive voltage drop terms, which are usually neglected in the literature, are considered in the calculation of the voltage amplitude in this study. The effect of nonlinear magnetizing inductance is also taken into account. Optimal reference points in the field-weakening region are calculated using either (19) or (20) depending on the operating condition.

As a summary, the optimal operating points diverge from the MTPA curve once the voltage limit is reached. The operating point will then be on the intersection point of the voltage limit with either torque curve or the current limit depending on the reference torque and speed. Further increasing the speed will push the operating point into the MTPV region.

D. Inverter Nonlinear Voltage Drop Compensation

The maximum attainable phase voltage is less than $V_{\rm dc}/\sqrt{3}$ due to inverter nonlinear voltage drop caused by its threshold voltage and voltage drop because of the dead-time effect. The linear inverter voltage drop by on-state resistance also degrades the maximum allowable phase voltage and its effects can be modeled by a series resistance in (20). A detailed explanation on the effect of inverter nonlinear voltage drop on the operating point trajectory of IM in the field-weakening region is given in [47]. In this article, the nonlinear voltage drops of the inverter are measured at standstill and at different d-axis current ($i_{\rm ds}$) levels, while d-axis is in alignment with phase A and $i_{\rm qs} = 0$ according to [48]. The inverter nonlinear voltage drop including the low-current nonlinearity, which is given in Fig. 5, is found by subtracting the stator resistive drop from the reference d-axis voltage. Note that the low-current nonlinearity is usually neglected in the existing literature and the inverter voltage drop is treated as a sign function [49], [50].

The dead-time effect varies with the current angle. To show the effect of the current angle on inverter voltage drop, d and q components of the inverter voltage drop ($V_{d\text{-drop}}$ and $V_{q\text{-drop}}$) are plotted versus the electrical angle in Fig. 6(a) and (b), respectively, for the current amplitude of 100 A. The results are given for three different current angles (0°, 45°, and 180°). The magnitude of the inverter voltage drop ($V_{m-\rm drop} = \sqrt{V_{d-\rm drop}^2 + V_{q-\rm drop}^2}$) is also given in Fig. 6(c).

It can be observed that although $V_{d\text{-drop}}$ and $V_{q\text{-drop}}$ both vary significantly with the current angle, the maximum and minimum values of the inverter voltage drop magnitude are independent of the current angle. Changing the current angle only affects the phase of the inverter voltage drop magnitude. For an accurate inverter voltage drop compensation, the variation

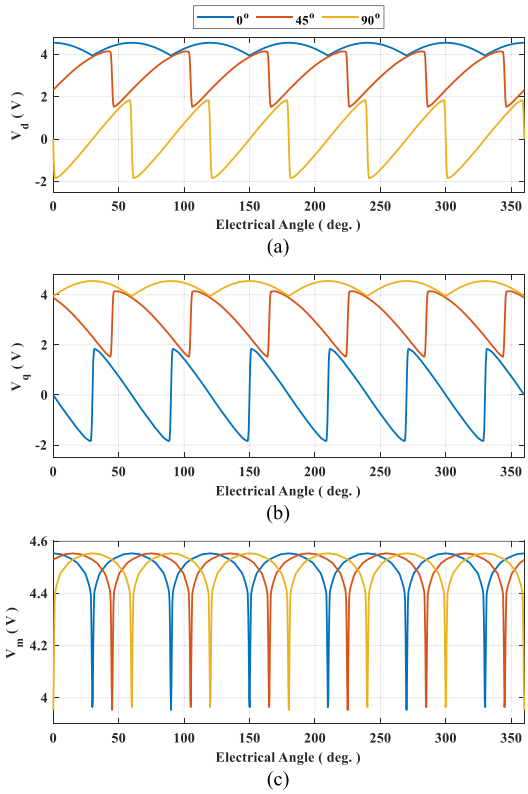

Fig. 6. Variation of inverter voltage drop versus electrical angle for different current angles. (a) $V_{d\text{-drop}}$. (b) $V_{q\text{-drop}}$. and (c) $V_{m\text{-drop}}$.

of both $V_{d\text{-drop}}$ and $V_{q\text{-drop}}$ with respect to the current angle should be considered separately, however, this will substantially increase the complexity and computational burden of the proposed control method. The magnitude of the inverter voltage drop always varies between a minimum and a maximum value for each current amplitude [51]. To guarantee that the reference operating points are always inside the voltage limit ellipse, only the maximum value of the inverter voltage drop is considered in calculation of the reference operating points. Hence, in this article, the maximum inverter voltage drop magnitude data for different current levels are stored in LUT to incorporate in the experimental implementation of the optimal tracking control algorithm. The maximum attainable voltage ($V_{\max}$) in (19) and (20) is calculated using

$$V_{\max} = \frac{V_{\text{dc}}}{\sqrt{3}} - |V_{m-\text{drop,max}}| \tag{21}$$

where $V_{m\text{-drop,max}}$ is the maximum amplitude of the inverter nonlinear voltage drop. The inverter voltage drop has a considerable impact on voltage curves of IM and ignoring it leads to a nonoptimal reference point outside the voltage curve and undesirable current ripples in the field-weakening operation.

IV. Proposed Online Optimal Tracking Control

A simple and straightforward algorithm is proposed in this article to control IM over the entire torque and speed ranges. In the proposed method, the torque-speed plane of the IM is divided into four regions with respect to the operating speed and torque by comparing the reference speed and the reference torque with the base speed and maximum achievable torque at the base speed, respectively. Once the region is detected, the corresponding calculation scheme is applied to find the optimal reference points (i_{ds}, i_{qs}).

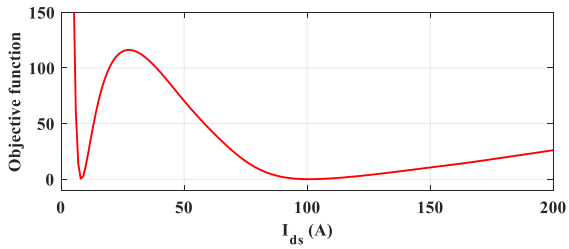

Fig. 7. Variation of the objective function versus i_{ds} to find the intersection of torque and voltage curves in the field-weakening region.

Note that golden section method is applied to solve all the nonlinear optimization problems online in MTPA, field-weakening, and MTPV regions. In order to use gradient-based minimization methods, like Newton's method, the objective function has to be convex. Otherwise, it might converge to an incorrect local minimum or maximum point. The variation of the objective function for finding the intersection of voltage and torque curves to determine the reference operating points in the field-weakening region versus i_{ds} is given in Fig. 7.

It can be observed that the objective function has local minimum and maximum points which will lead to convergence to an incorrect solution if derivative-based methods (like Newton's method) is used. Therefore, golden section method, which is a 1-D search algorithm and has a faster convergence rate compared to other 1-D derivative-free search methods, is implemented to solve the nonlinear equations in this article. Golden section method starts with assuming an initial interval ($[a, b]$) which contains the solution for the minimization or maximization problem ($f(x) = 0$). Then, two intermediate points (x_1 and x_2) are calculated using the well-known golden section ratio ($d = \frac{\sqrt{5}-1}{2}$) as $x_1 = a + (1 - d)(b - a)$ and $x_2 = a + d(b - a)$. The interval and the intermediate points are iteratively updated depending on the values of $f(x_1)$ and $f(x_2)$. If ($f(x_1) < f(x_2)$), then $b = x_2$, $x_2 = x_1$, and $x_1 = a + (1 - d)(b - a)$. Otherwise, in case ($f(x_1) \geq f(x_2)$), the interval and the intermediate points are updated as $a = x_1$, $x_1 = x_2$, and $x_2 = a + d(b - a)$. If the desired stopping criteria ($b - a \leq \varepsilon$), in which ε is the desired tolerance for the solution, is met, the algorithm stops and the solution is $x_{\text{optimal}} = \frac{a+b}{2}$. Otherwise, the algorithm continues by repeating the above-mentioned repetitive process. In this article, the nonlinear equations are solved to determine the reference currents, hence, the initial interval is assumed to be $[0, I_{\max}]$. Furthermore, the desired stopping criteria is set to $\varepsilon = 0.1$ A.

A. Flowchart of the Proposed Optimal Tracking Control

At the initialization stage, it is required to calculate the torque (T_A) and the synchronous speed ($n_{s,A}$) at the intersection of

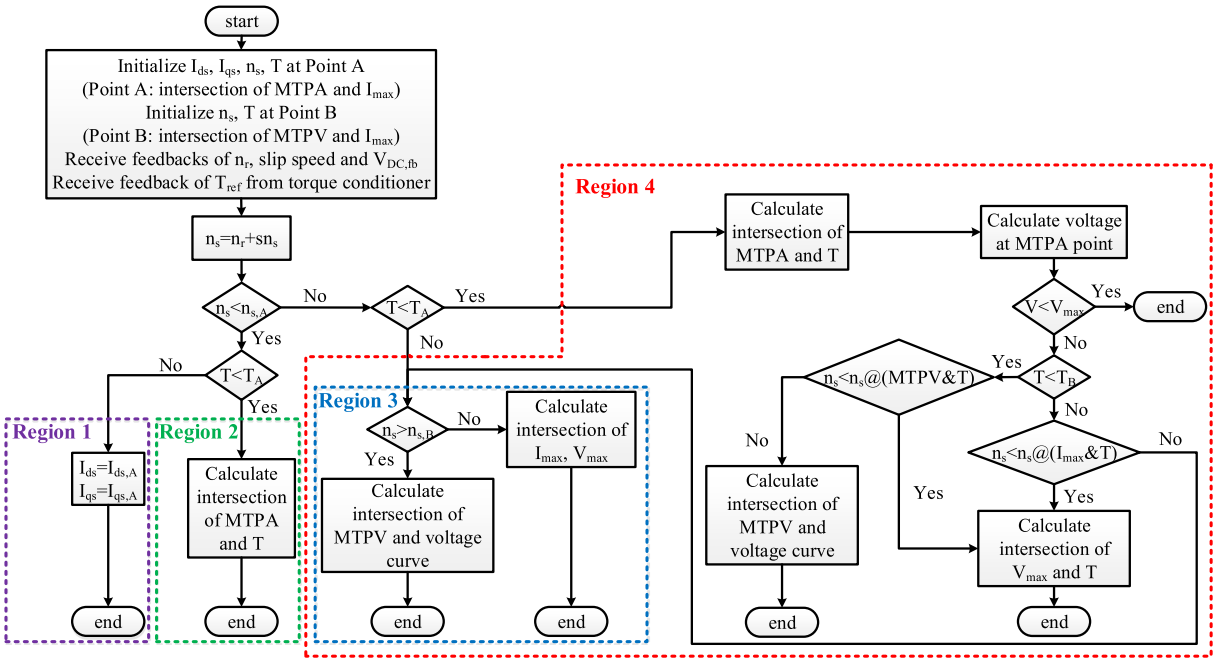

Fig. 8. Flowchart of the proposed online optimal tracking control.

MTPA curve and the maximum current limit, which is shown by A in Fig. 2. The intersection point ($I_{\mathrm{ds,A}}$, $I_{\mathrm{qs,A}}$) is found by solving

$$\begin{cases} i_{\mathrm{qs}} = i_{\mathrm{ds}}\sqrt{\dfrac{1}{1+\frac{\dot{L}_m}{L_m}i_{\mathrm{ds}}}} \\ i_{\mathrm{ds}}^2 + i_{\mathrm{qs}}^2 = I_{\mathrm{max}}^2. \end{cases} \tag{22}$$

Then, both torque (T_A) and the synchronous speed ($n_{s,A}$) corresponding to the maximum voltage at point A are calculated using torque in (5) and voltage limit equation ($v_{\mathrm{ds}}^2 + v_{\mathrm{qs}}^2 = V_{\mathrm{max}}^2$), respectively. Note that this calculation is required to be done only once as long as the dc-link voltage stays constant. T_A is the maximum torque which can be developed by IM under the maximum current limit which ensures safe operation of both inverter and machine. Moreover, $n_{s,A}$ is the base speed of the machine. Further increasing the speed will reduce the maximum torque which can be produced by IM, and the machine will enter into the constant power region. Note that, because *d*–*q* equations are written in a synchronously rotating reference frame, ω is the synchronous speed in all the equations in this article. Furthermore, the torque (T_B) and the synchronous speed ($n_{s,B}$) at the intersection point of MTPV and the maximum current curve, as shown by B in Fig. 2, are also calculated as a part of initialization. Stator *d*- and *q*-axis currents at point B ($I_{ds,B}$, $I_{\mathrm{qs,B}}$) are calculated by solving

$$\begin{cases} \dfrac{\zeta\dot{\zeta}T_{\mathrm{ref}}^2}{k^2L_m^2i_{\mathrm{ds}}^2} + L_s^2 i_{\mathrm{ds}} + L_s\dot{L}_s i_{\mathrm{ds}}^2 - \dfrac{\zeta^2 T_{\mathrm{ref}}^2}{k^2L_m^3 i_{\mathrm{ds}}^3}\left(\dot{L}_m i_{\mathrm{ds}} + L_m\right) = 0 \\ i_{\mathrm{ds}}^2 + i_{\mathrm{qs}}^2 = I_{\mathrm{max}}^2. \end{cases} \tag{23}$$

Then, the torque and the synchronous speed corresponding to the maximum voltage at point B are calculated using torque and voltage limit equations. This reference point B along with A is used to detect the operating regions and subregions to generate corresponding optimal reference points. The reference torque is fed by the torque conditioner to the optimization-based reference generator. The torque conditioner monitors the speed feedback and dc-link voltage and generates the best torque possible at each particular scenario by considering the system dynamic constraints. The flowchart of the proposed online optimal tacking control is presented in Fig. 8.

After the initialization stage, the synchronous speed of IM is estimated using the measured rotor speed (n_r) and the estimated slip-speed (sn_s) as

$$n_s = n_r + (sn_s)\,. \tag{24}$$

The slip-speed should be estimated to calculate the reference synchronous speed. As ($\lambda_{\mathrm{qr}} = 0$) under FOC, and using λ_{qr} equation in (2), we get

$$i_{\mathrm{qr}} = -\frac{L_m}{L_r}i_{\mathrm{qs}}. \tag{25}$$

By rewriting the rotor q-axis voltage equation in (1) under FOC condition gives

$$0 = R_r i_{\mathrm{qr}} + (s\omega_s)\,(L_m i_{\mathrm{ds}}) \tag{26}$$

where ($s\omega_{\mathrm{s}} = \omega_{\mathrm{s}} - \omega_{\mathrm{me}}$) is the slip-speed in rad/s. By rearranging (26) and using (25), the slip speed can be estimated using

$$s\omega_s = \frac{R_r i_{\mathrm{qs}}}{L_r i_{\mathrm{ds}}} = \frac{i_{\mathrm{qs}}}{\tau_r i_{\mathrm{ds}}} \tag{27}$$

where τ_r is the rotor time constant.

It can be observed from Fig. 8 that after determination of the operating region by comparing the synchronous speed and the reference torque with $n_{s,A}$ and T_A, respectively, the corresponding calculations are carried out to generate the optimal reference currents. The calculation scheme for each region is explained as follows.

1) Region 1 ($n_s \leq n_{s,A}$ and $T_{\rm ref} \leq T_A$): In this region, the optimal reference points are the intersection point of MTPA curve and the reference torque curve. As there is no need to consider voltage and current constraints in this region, the optimal points are generated to minimize stator current amplitude by satisfying the MTPA condition. The reference operating points are calculated by solving

$$\begin{cases} i_{\rm qs} = i_{\rm ds}\sqrt{\dfrac{1}{1+\dfrac{\dot{L}_m}{L_m}i_{\rm ds}}} \\ T_{\rm ref} = kL_m i_{\rm ds} i_{\rm qs}. \end{cases} \tag{28}$$

Note that when $T_{\rm ref} = T_A$ the operating point is the point A shown in Fig. 2 where the IM delivers its maximum torque.

2) Region 2 ($n_s \leq n_{s,A}$ and $T_{ref} > T_A$): In region 2, as the reference torque is bigger than the maximum torque production capability of IM (T_A), the reference torque cannot be tracked anymore, and the optimal operating point is the intersection of the MTPA curve and the maximum current limit (point A) which is calculated by using (22).

3) Region 3 ($n_s > n_{s,A}$ and $T_{ref} > T_A$): Because the speed is higher than $n_{s,A}$ in this region, the operating points are found considering the voltage constraint. As the reference torque is bigger than T_A, the optimal reference points are the intersection of the voltage curve and the maximum current limit as long as $n_s < n_{s,B}$. Hence, the reference operating points are calculated by solving (20). If the speed increases beyond $n_{s,B}$, the IM operates in the MTPV region. Hence, the reference points are found to be the intersection of the MTPV and the voltage limit curves which are calculated using

$$\begin{cases} \dfrac{\zeta\dot{\zeta}T_{\rm ref}^2}{k^2L_m^2 i_{\rm ds}^2} + L_s^2 i_{\rm ds} + L_s\dot{L}_s i_{\rm ds}^2 \\ \quad - \dfrac{\zeta^2 T_{\rm ref}^2}{k^2 L_m^3 i_{\rm ds}^3}\left(\dot{L}_m i_{\rm ds} + L_m\right) = 0 \\ \left(R_s i_{\rm ds} - \omega\lambda_{\rm qs}\right)^2 + \left(R_s i_{\rm qs} + \omega\lambda_{\rm ds}\right)^2 = V_{\rm max}^2. \end{cases} \tag{29}$$

Similar to region 2, the reference torque cannot be tracked in this region due to current and voltage limitations.

4) Region 4 ($n_s > n_{s,A}$ and $T_{ref} \leq T_A$): In region 4, if the voltage at the intersection of the MTPA and reference torque curves, which is found using (28), is less than the maximum voltage limit, the operating point is on the MTPA curve. Otherwise, the optimal points are found by taking the voltage constraint into the account. In case the reference torque is smaller than T_B, the synchronous speed corresponding to the maximum attainable voltage is calculated at the intersection of the MTPV and the reference torque curves (n_s@(MTPV&T)). The intersection point is calculated from

$$\begin{cases} \dfrac{\zeta\dot{\zeta}T_{\rm ref}^2}{k^2L_m^2 i_{\rm ds}^2} + L_s^2 i_{\rm ds} + L_s\dot{L}_s i_{\rm ds}^2 \\ \quad - \dfrac{\zeta^2 T_{\rm ref}^2}{k^2 L_m^3 i_{ds}^3}\left(\dot{L}_m i_{\rm ds} + L_m\right) = 0 \\ T_{\rm ref} = kL_m i_{\rm ds} i_{\rm qs}. \end{cases} \tag{30}$$

Then, the synchronous speed at the intersection point corresponding to the maximum attainable voltage is calculated using the voltage limit equation. If it is higher than the reference synchronous speed, the optimal operating point is the intersection of the voltage limit and the torque curves, which is found by solving (19). Otherwise, the operating point is in the MTPV region at the intersection of the MTPV and voltage limit curves which is calculated using (29). In case the reference torque is bigger than T_B, the synchronous speed corresponding to the maximum attainable voltage at the intersection of the reference torque and the maximum current curves (n_s@($I_{\rm max}$&T)) is calculated. The intersection point is found by solving

$$\begin{cases} i_{\rm ds}^2 + i_{\rm qs}^2 = I_{\rm max}^2 \\ T_{\rm ref} = kL_m i_{\rm ds} i_{\rm qs}. \end{cases} \tag{31}$$

Then, the synchronous speed at the intersection point corresponding to the voltage limit is found by using the maximum voltage ellipse equation ($v_{\rm ds}^2 + v_{\rm qs}^2 = V_{\rm max}^2$). If it is higher than the reference synchronous speed, the optimal operating point is the intersection of the reference torque and the voltage limit curves which is found from (19). Otherwise, the operating point is determined by using the approach described for region 3.

In order to consider the effect of temperature variation on the stator winding resistance in the proposed algorithm, the resistance value is updated based on the feedback from the stator measured temperature. At any temperature (θ), the stator resistance is calculated using

$$R_{s,\theta} = R_{s,\,25^\circ{\rm C}}\left(1 + \alpha\left(\theta - 25\right)\right) \tag{32}$$

where α is the temperature coefficient of resistivity for copper ($\alpha = 0.0039$ (1/°C)). Therefore, the resistance is updated online as the stator temperature varies.

B. Stability and Smooth Operation of the Proposed Controller

The proposed optimal control has two parts: (1) Optimization-based optimal current reference generator for the entire torque-speed range, and (2) Linear (PI) current controllers. The stability of linear feedback controllers is obvious by assuming bounded parameter variations. The optimization-based optimal reference current generator does not affect the stability of the feedback control system as it is just a reference generator. A well-tuned feedback control system (PI controller in this case) tracks the reference currents effectively as long as there is a meaningful reference current from the optimization. However, if the optimization diverges significantly, it can result in impractical reference currents which the PI controller cannot track well and may result in instability. So, in this article, investigating

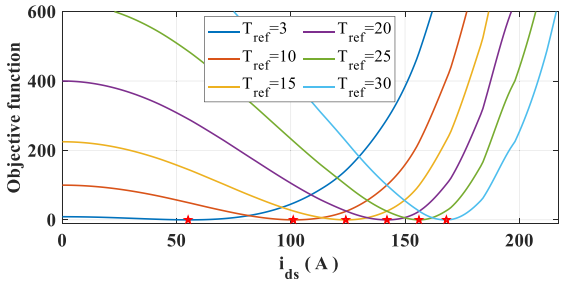

Fig. 9. Convexity of the objective function in the MTPA region.

the convergence of the current reference generator in the entire torque-speed range is of great importance, as the stability of the linear feedback system is obvious. As 1-D golden-section search algorithm is implemented in this article to solve all nonlinear equations, the objective functions need to be convex over the entire stator d-axis current range $[0, I_{\max}]$.

The variation of the objective function versus $i_{\rm ds}$ in the MTPA region for six different reference torque levels are shown in Fig. 9. Note that the minimum of the objective functions (solution) is depicted by red stars on the figure. It can be observed that the objective functions are all convex in the entire torque and current ranges. Hence, the convergence of the current reference generator is proved in the MTPA region. Further analysis reveals that the objective functions used to calculate the optimal current references in the entire operating speed and torque ranges of the test IM are all convex. Due to space limitations, the proof of convexity for other nonlinear equations used in the optimal current reference generation has not been given here.

To investigate the smooth operation of the proposed controller between MTPA and field-weakening regions, the optimal reference points are found by golden-section-based optimization over the entire operating speed and torque ranges of the test IM. Note that the maximum operating speed of the test IM is 5000 rpm, however, the simulation results are shown up to around 10000 rpm to represent the performance of the proposed control algorithm in the deep field-weakening region. The calculated reference $i_{\rm ds}$ and $i_{\rm qs}$ are presented in Fig. 10(a) and (b), respectively. It can be observed that at the lower speeds the reference points are on the MTPA curve. As the speed increases, $i_{\rm ds}$ reduces and IM operates in the field weakening region as seen in Fig. 10(a). On the other hand, $i_{\rm qs}$ increases to track the desired reference torque until the current reaches the limit. The smooth operation of the proposed controller between MTPA and field-weakening regions is seen from Fig. 10(a) and (b). The maximum torque production capability of the IM with the proposed optimal control algorithm is shown in Fig. 11. IM can deliver the maximum torque of 30.3 Nm up to its base speed ($n_{s,A} = 2776$ rpm, speed at the intersection of MTPA, and the maximum current limit) in the constant-torque region. Then, the torque production capability is reduced in the field-weakening region and IM enters constant-power region. Note that as the speed at the intersection of MTPV and the maximum current limit ($n_{s,B} = 14\,995$ rpm) is much higher than maximum speed of the test IM, therefore it cannot operate in the MTPV region.

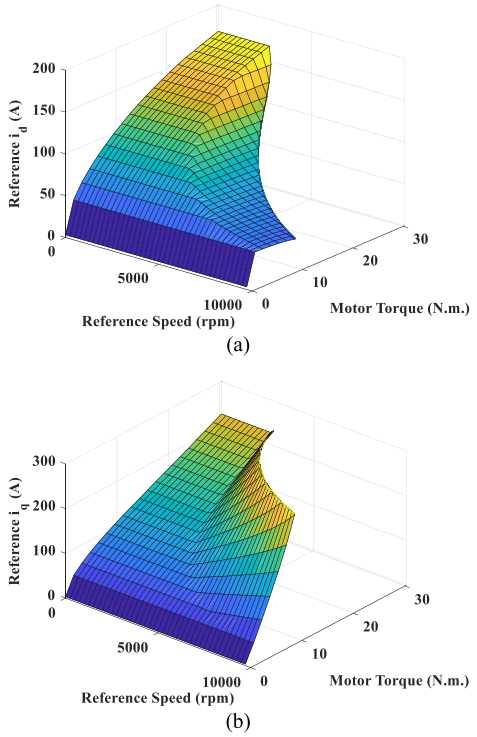

Fig. 10. Optimal reference currents over entire operating speed and torque ranges. (a) Reference $i_{\rm ds}$. (b) Reference $i_{\rm qs}$.

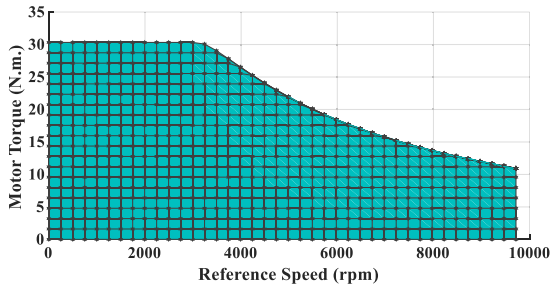

Fig. 11. Torque production capability of the test IM with the proposed optimal control algorithm.

V. Experimental Results

The proposed method is experimentally verified on a 4.7-kW, 4-pole, three-phase IM drive. A surface permanent magnet (SPM) motor operates as the dyno in a back to back configuration with the test IM to control the speed. Two 400 V, 200 A off the shelf BorgWarner Gen 5 Size 9 voltage source inverters/controllers with liquid cooling are employed. The dc-link voltage is set to 55 V. The experimental setup is given in Fig. 12. The frequency of the optimal control reference generation block is 4 kHz. The current sampling frequency and the switching frequency are both 8 kHz.

The block diagram of the experimental setup is presented in Fig. 13. The conventional speed control is applied to SPM to hold the shaft speed at the desired reference ($n_{\rm ref}$). IM operates with the proposed online optimal control. The optimal control unit generates the optimal reference currents ($i_{\rm ds}$, $i_{\rm qs}$) corresponding

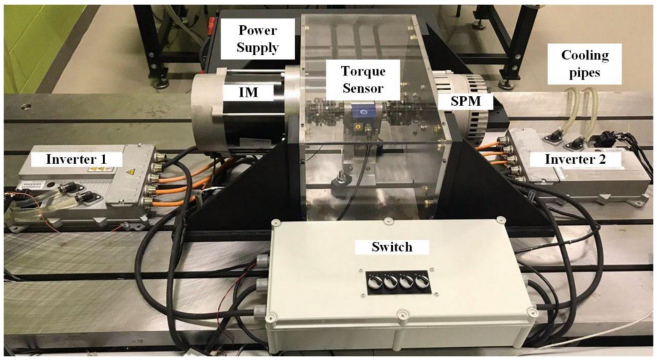

Fig. 12. Experimental setup.

to the reference torque ($T_{\rm ref}$) and measured rotor speed (n_r), which is kept equal to the reference speed ($n_{\rm ref}$) by SPM. The variations in dc-link voltage are also considered in the proposed optimal control algorithm with feedback from the measured dc-link voltage. The slip speed is estimated in the "slip estimation" block from (25) using both reference $i_{\rm ds}$ and $i_{\rm qs}$. Note that the golden section method is implemented to solve all nonlinear equations in the optimal control unit online. The experimental results for different reference speed and reference torque levels are presented in this section.

A. Experimental Results in the Entire Speed and Torque Ranges

The operation of the proposed controller in MTPA region is presented in Fig. 14. The shaft speed is held at $n_{\rm ref} = 500$ rpm by the SPM, and the torque commands are applied from 0 to 40 Nm with 2 Nm steps. The optimal reference points are on the MTPA curve as the IM operates in the constant-torque region (low-speed region). Good tracking capability of the current controller can be seen from Fig. 14(c). The desired reference torque and measured torque are both given in Fig. 14(b). The reference torque in SPM side, shown by T^* in Fig. 13, is also given. It can be observed that measured torque is slightly lower than the reference torque, especially at higher torque levels. This torque error is due to core and friction losses of IM which are neglected in generating the reference currents in the proposed method. The reference torque cannot be tracked anymore once the current limit is reached ($t = 80$ s in Fig. 14(c)). So, the IM operates on the boundary of the current limit on the MTPA curve. It should be noted that because $n_s < n_{s,A}$ in this experiment, the IM operates in regions 1 and 2. Both the reference and the measured operating points are shown on the $i_{\rm ds}$–$i_{\rm qs}$ plane in Fig. 14(d). It is seen that the optimal points are on the nonlinear MTPA curve. As the main purpose of this experiment is to show the performance of the controller in the entire MTPA region, the saturation limit is not taken into account. The optimal operating points trajectory will be changed as shown by black arrows in Fig. 14(d), if the saturation is considered.

To investigate the operation of the proposed optimal tacking control at higher speeds, the speed is kept constant at 4000 rpm by the SPM, and the torque steps are applied (0–34 Nm with the steps of 2 Nm). The results are presented in Fig. 15. It can be observed from Fig. 15(c) that, the current ripples increase compared to MTPA operation as the operating points are on the voltage boundary. As seen in Fig. 15(b), the reference torque is tracked until the maximum current limit is reached ($t = 50$ s in Fig. 15(c)). As discussed earlier, the steady-state torque error is due to the negligence of core and friction losses in the proposed optimal tracking control algorithm. From the operating point trajectory in Fig. 15(e), it can be seen that the operating points are on the MTPA curve at lower commanded torques. Then, by increasing the commanded torque, the IM enters the field-weakening region and the operating points are on the constant voltage curve corresponding to the synchronous speed of 4000 rpm. After $t = 20$ s, IM operates on the voltage boundary as shown in Fig. 15(d) and consequently the current ripples are bigger compared to the MTPA region. Note that the voltage curves in the $i_{\rm ds}$–$i_{\rm qs}$ trajectory shown in Fig. 15(e) are plotted for different synchronous speeds and without considering inverter voltage drop. Moreover, as the rotor speed is set at 4000 rpm, the synchronous speed becomes higher depending on the slip speed of the IM. Furthermore, the voltage ellipses shrink even further due to the inverter voltage drop. Once the current limit is reached, the optimal reference point is the intersection point of the voltage and current limits in which IM delivers the maximum attainable torque at 4000 rpm. Before reaching the current limit, the optimal reference points are at the intersection points of torque and voltage curves. Due to slight variations in the rotor speed (around 65 rpm peak to peak), the synchronous speed and consequently the voltage curves vary. Therefore, the operating points are on the constant torque curve and within a band of voltage curves corresponding to the minimum and maximum synchronous speeds. In this experiment, IM is in region 4 as long as $T_{\rm ref} \leq T_A$. It operates in region 3 with a further increase of the reference torque beyond T_A.

The performance of the controller under reference speed step commands is investigated by applying the speed steps under a constant load torque of 15 Nm. The experimental results are shown in Fig. 16. The command speed is varied from 600 to 5000 rpm with steps of 200 rpm as shown in Fig. 16(a). It can be seen from Fig. 16(b) that load torque is kept constant at 15 Nm, and IM can deliver the reference torque in the entire speed range. Reference currents are very well tracked by the measured currents as seen in Fig. 16(c). The operating points are on the intersections of MTPA curve and the constant torque curve of 15 Nm at lower speeds (until 2800 rpm which happens around $t = 55$ s). At the speeds beyond 2800 rpm, the operating points are found by calculating the intersection of the torque curve of 15 Nm and voltage curves corresponding to each speed. It can be seen from Fig. 16(c) that after $t = 55$ s the $i_{\rm ds}$ reduces and IM enters the field-weakening region, where IM operates on the voltage boundary as shown in Fig. 16(d). Before $t = 55$ s, where the IM operates in the MTPA region, the voltage amplitude is less than the voltage limit (Fig. 16(d)) and there are no ripples on the reference currents. However, after $t = 55$ s, IM operates on the voltage boundary in the field weakening region and the operating points are the intersection of voltage curve with torque curve. From Fig. 16(c), very small ripples are observed on the

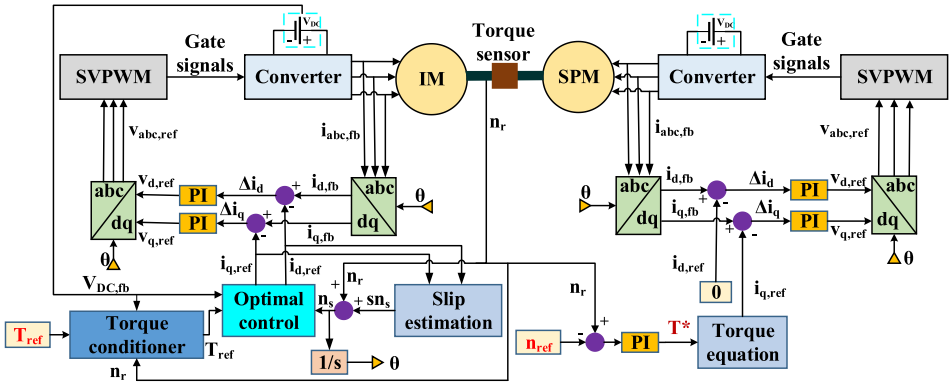

Fig. 13. Block diagram of the experimental setup.

reference currents in this region due to variations of the voltage curve as a result of small speed ripples. The operating point trajectory is given in Fig. 16(e). Note that the operating points do not reach the current limit boundary in the entire speed range under $T_{\text{ref}} = 15$ Nm.

The experimental results with the speed step commands under the reference torque of 25 Nm are presented in Fig. 17. The similar speed steps from 600 to 5000 rpm with the steps of 200 rpm are applied, as shown in Fig. 17(a). It can be observed from Fig. 17(e) that the operating point is at the intersection of MTPA and the constant torque curve of 25 Nm at lower speeds (till $t \approx 50$ s in Fig. 17(c)). As the speed increases beyond 2600 rpm, IM enters field-weakening region, and the optimal reference points are found to be the intersection of torque curve of 25 Nm and the corresponding voltage curve ($t \approx 50$–65 s in Fig. 17(c)). Hence, IM operates in the voltage boundary (shown in Fig. 17(d)) and delivers the reference torque until the current limit is reached. On the current limit boundary, the operating points are on the intersection of the current limit circle with the corresponding voltage curve ($t > 65$ s in Fig. 17(c)). After $t \approx 65$ s, the reference torque cannot be tracked anymore, as seen in Fig. 17(b), and IM delivers the maximum attainable torque limited by both current and voltage constraints.

Neglecting the effect of iron loss in generating the reference operating points in the proposed control algorithm may result in some torque errors in the operating regions where iron loss is dominant. The iron loss (P_{iron}) is calculated using (33) by subtracting output power (P_{out}), copper losses (P_{cu}), and friction losses (P_{friction}) from the input power (P_{in}):

$$\begin{aligned} P_{\text{iron}} &= P_{\text{in}} - P_{\text{out}} - P_{\text{cu}} - P_{\text{friction}} \\ &= \sum_{i=1}^{3} V_i I_i \cos(\varphi_i) - T_{\text{out}}\omega_r - R_s \sum_{i=1}^{3} I_i^2 - T_{\text{friction}}\omega_r \end{aligned} \tag{33}$$

where V_i, I_i, $\cos(\varphi_i)$, T_{out}, T_{friction}, and ω_r stand for phase rms voltage, phase rms current, phase power factor, output torque, friction torque, and rotor angular speed in rad/s,respectively. In order to investigate the effect of iron loss on torque control performance, the iron loss is measured at 4000 rpm (high speed) under high load ($T_{\text{ref}} = 17$ Nm). Note that 17 Nm is the maximum achievable torque at 4000 rpm. The input power is measured using the power analyzer to be 7472 W. The measured output torque is 15.73 Nm. The friction torque at 4000 rpm is measured using the torque transducer to be around 0.39 Nm. Finally, the core loss is calculated to be $P_{\text{iron}} = 492.1$ W. The torque corresponding to the iron loss (T_{iron}) is calculated using

$$T_{\text{iron}} = \frac{P_{\text{iron}}}{\omega_r} = \frac{492.1}{4000 \times \frac{2\pi}{60}} = 1.17 \text{ Nm}. \tag{34}$$

It can be observed that the torque corresponding to the iron loss is only 7.4% of the measured torque. In order to show the validity of iron loss calculations, the reference torque is compensated by 1.17 Nm. The experimental results at 4000 rpm and under reference torque of 17 Nm are presented in Fig. 18. It can be observed that there is a torque error before considering the iron loss effect. Once the reference torque is compensated by the T_{iron} at $t = 10$ s, the error between the desired torque of 17 Nm and the measured torque is significantly reduced.

As stated earlier, two off-the-shelf BorgWarner Gen5 Size9 inverter and controllers, provided by the industrial partner, are used in this study. The control and switching frequencies are 4 and 8 kHz, respectively. Changing control and switching frequency can affect the performance of the proposed control strategy. Increasing the frequency with the proposed optimal control to 10 kHz, which is commonly used in industrial drives, will lead to the faster update of the reference operating points. This might even result in a reduction of the current ripples, especially in the field-weakening region.

B. Experimental Results Under Severe Speed and Torque Variations

In order to evaluate the performance of the proposed controller under severe torque dynamics in the MTPA region, reference torque steps of 9 Nm (rated torque) are applied while the shaft speed is held at 500 rpm by the dyno machine. The results are presented in Fig. 19. It can be observed that the proposed controller is capable of controlling IM in the MTPA region under severe reference torque dynamics. Note that after $t = 40$ s, the

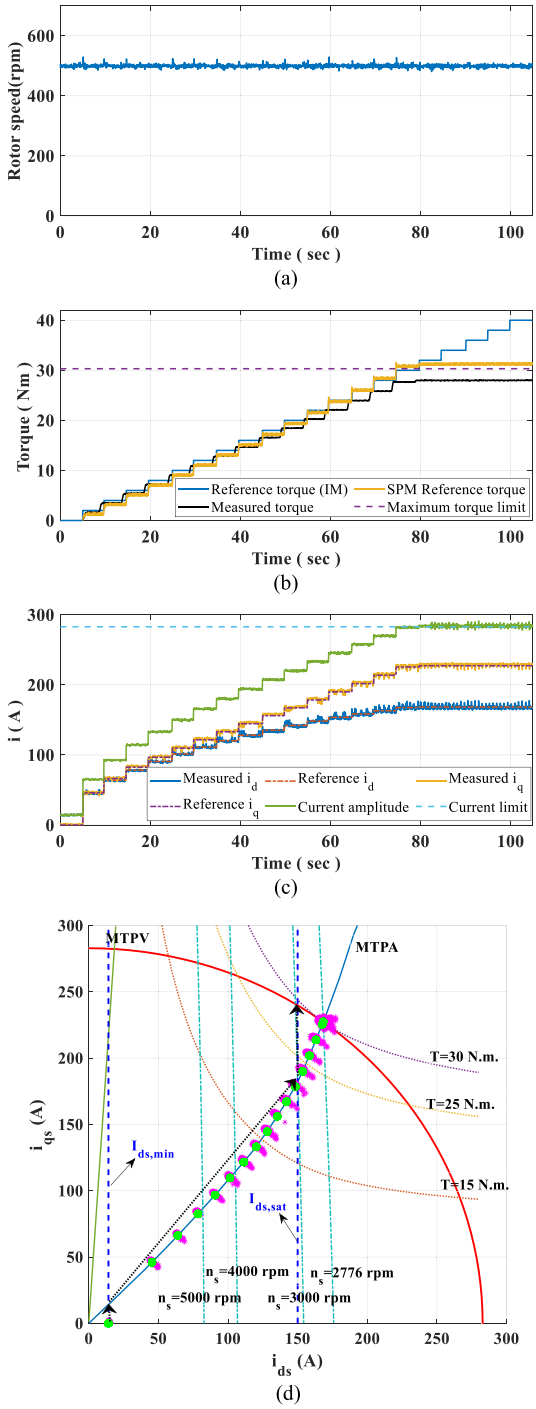

Fig. 14. Experimental results at 500 rpm in MTPA region with torque step commands. (a) Measured speed. (b) Torque. (c) Current. (d) Operating points trajectory.

reference torque is bigger than the maximum torque limit of IM and the operating points are selected to be the intersection of MTPA and maximum current limit. Hence, after $t = 40$ s, the stator current is equal to the maximum current limit, as shown in Fig. 19(b).

To analyze the performance of the proposed controller under severe speed dynamics, two speed steps of 2000 rpm (500 to

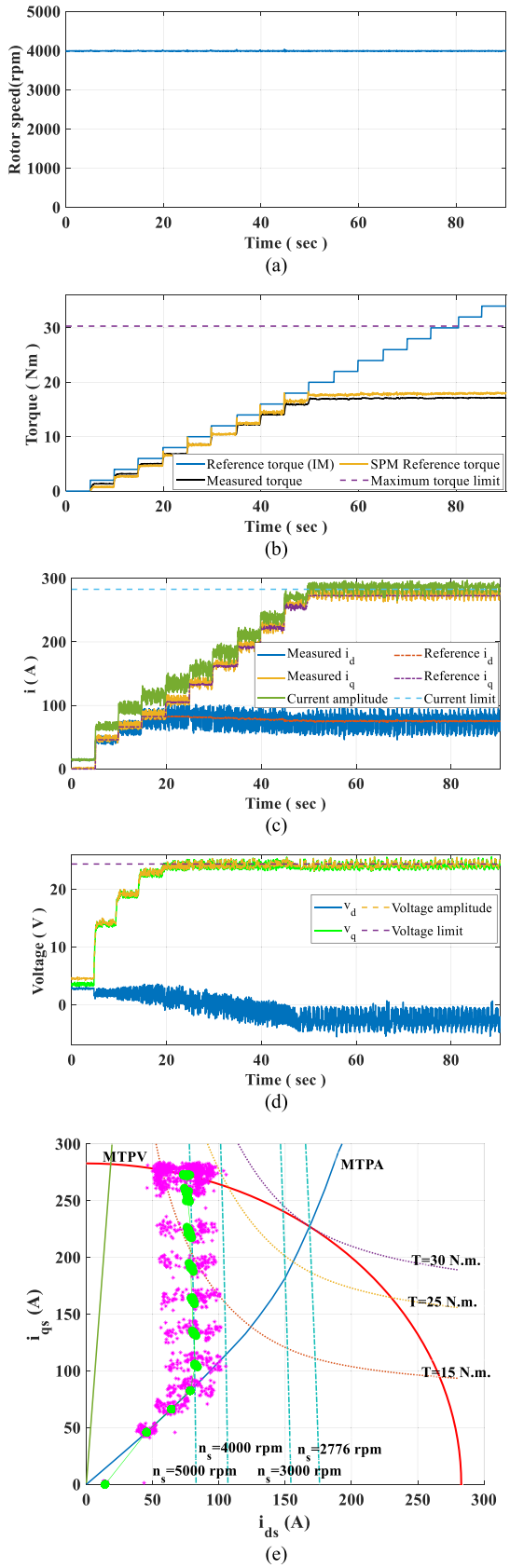

Fig. 15. Experimental results at 4000 rpm with toque step commands. (a) Measured speed. (b) Torque. (c) Current. (d) Voltage. (e) Operating points trajectory.

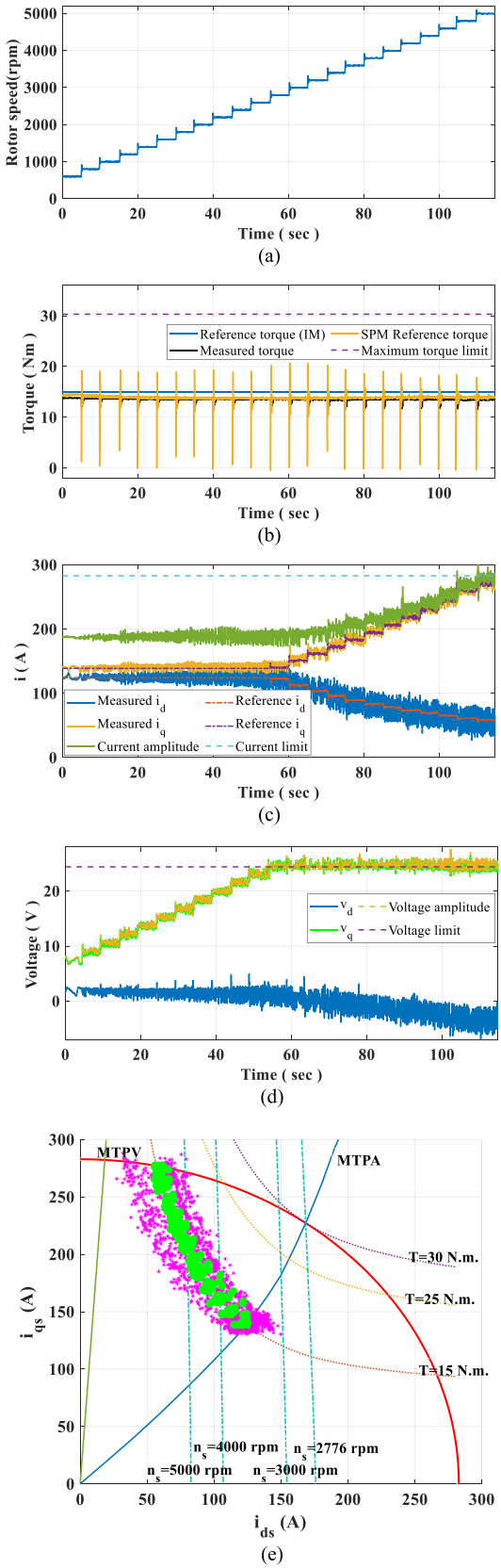

Fig. 16. Experimental results under load torque of 15 Nm with speed step commands. (a) Measured speed. (b) Torque. (c) Current. (d) Voltage. (e) Operating points trajectory.

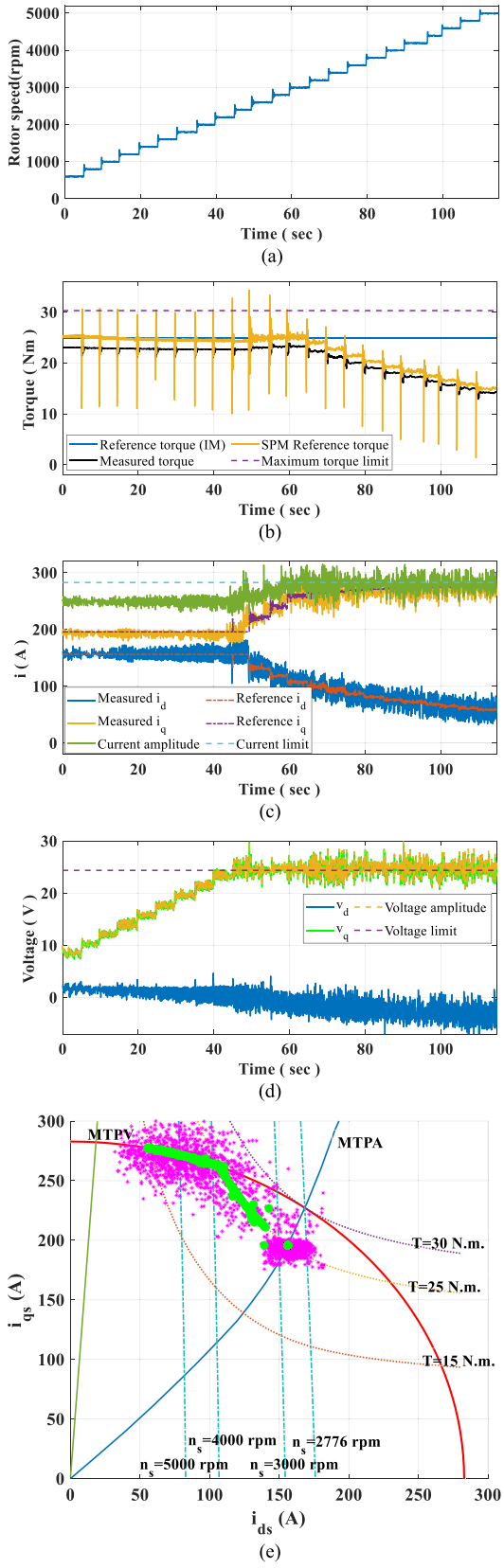

Fig. 17. Experimental results under load torque of 25 Nm with speed step commands. (a) Measured speed. (b) Torque. (c) Current. (d) Voltage. (e) Operating points trajectory.

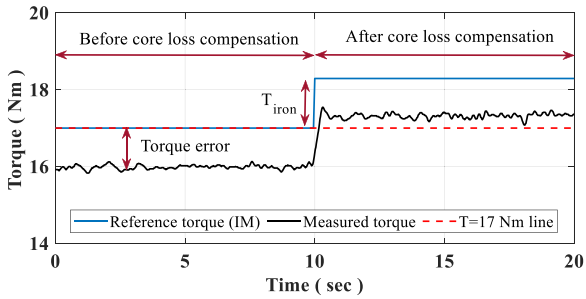

Fig. 18. Experimental results on the effect of iron loss on torque error.

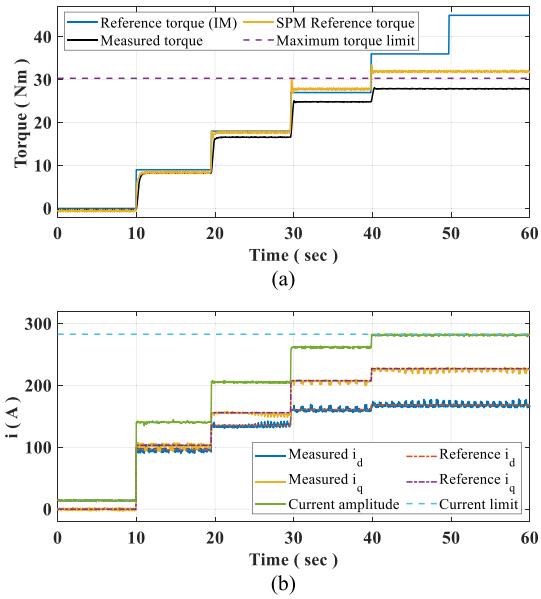

Fig. 19. Experimental results at 500 rpm in MTPA region under severe reference torque dynamics. (a) Torque. (b) Current.

2500 rpm, and 2500 to 4500 rpm) are applied while the reference torque is 15 Nm. The experimental results are presented in Fig. 20. It can be seen that the reference torque can be followed in the entire speed range. The operating points are on the MTPA curve until $t = 20$ s. Then, IM enters the field-weakening region where it operates on the voltage limit, as shown in Fig. 20(d). The operating points at 4500 rpm are the intersection of torque and voltage limit curves.

C. Four-Quadrant Operation of the Proposed Controller

In this section, the experimental results are provided to show the capability of the proposed method in controlling the IM drives in both motoring and generating modes. The experimental results under load torque of 15 Nm and applied speed step commands (-600 to -3200 rpm with the steps of -200 rpm) are presented in Fig. 21. Note that IM is operating in the generating mode in this test. It can be observed that the controller is capable of controlling the IM to deliver the desired torque on the shaft, as shown in Fig. 21(b). Good tracking capability of the current

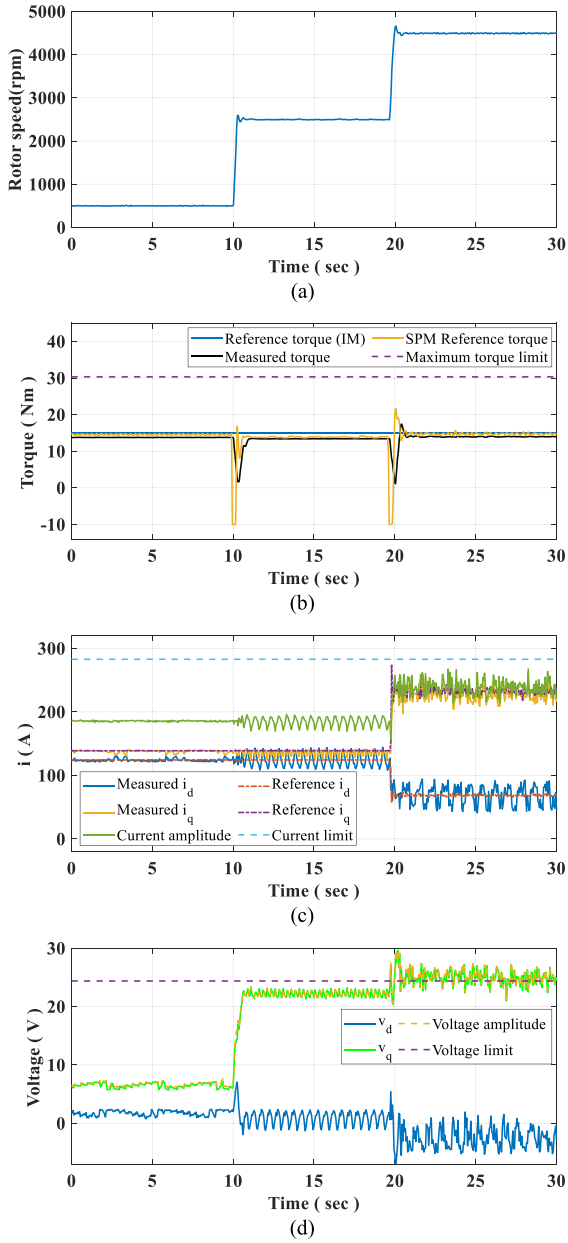

Fig. 20. Experimental results under reference torque of 15 Nm with severe speed dynamics. (a) Mechanical speed. (b) Torque. (c) Current. (d) Voltage.

controllers can be seen from Fig. 21(c). The variation of d and q axes voltages at different rotor speeds are shown in Fig. 21(d).

D. Effect of Parameter Variations on the Performance of the Proposed Control Method

Considering the effect of motor parameter variations [52]–[54] on the performance of the controller is of great importance. The variation of the magnetizing inductance (L_m) due to saturation has been considered in this article using the measured L_m LUT shown in Fig. 1. The variation of the stator resistance versus temperature is also considered by updating the resistance value based on the feedback from the stator measured

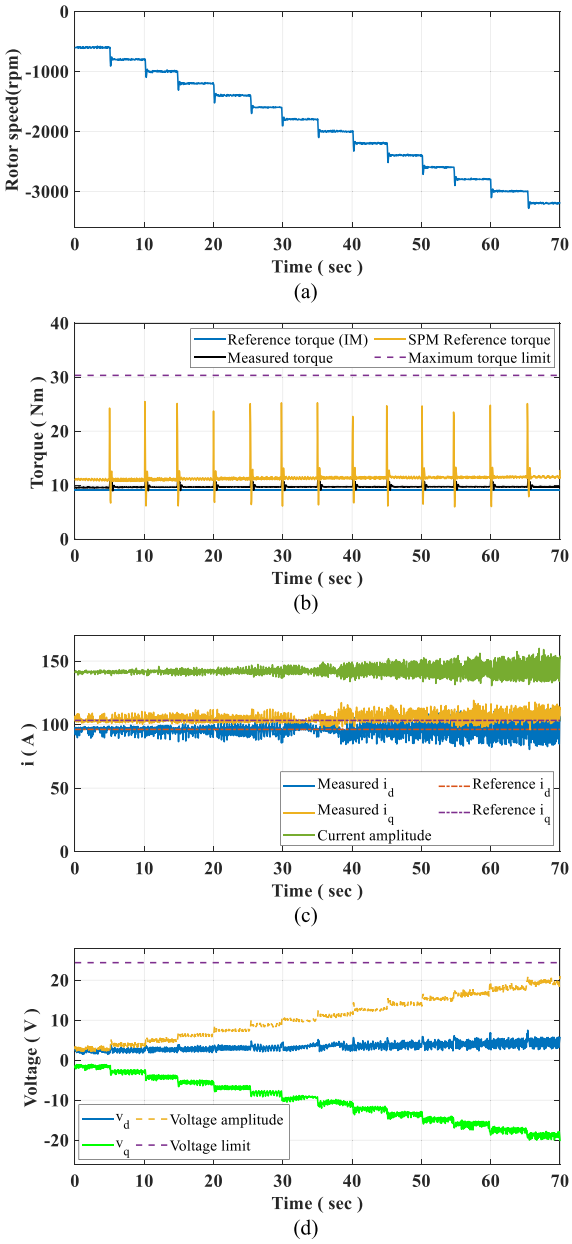

Fig. 21. Experimental results in negative speed and positive torque region. (a) Mechanical speed. (b) Torque. (c) Current. (d) Voltage.

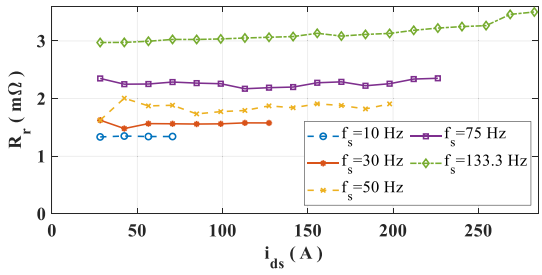

Fig. 22. Variation of rotor resistance versus $i_{\rm ds}$ and excitation frequency.

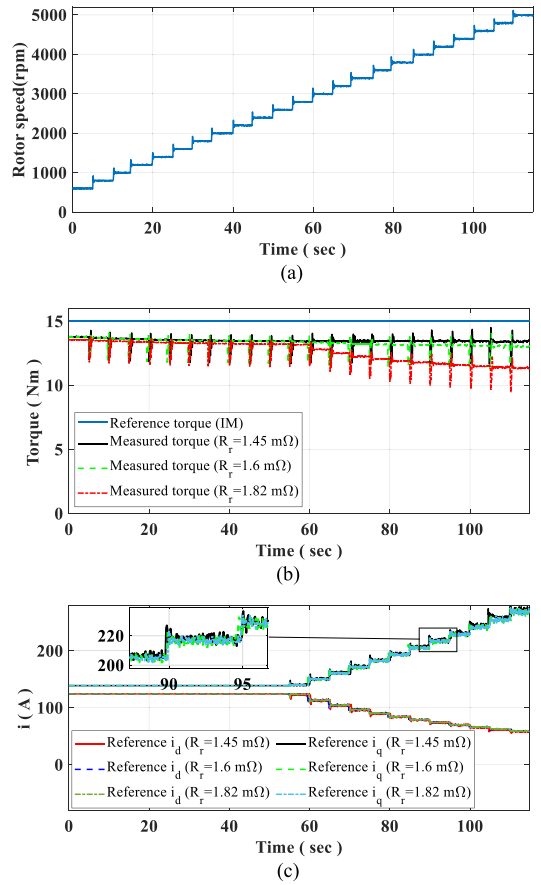

Fig. 23. Experimental results with speed steps under load torque of 15 Nm for three different rotor resistance values. (a) Mechanical speed. (b) Torque. (c) Current.

temperature as discussed earlier. Rotor resistance can vary with frequency. Rotor frequency is equal to the slip frequency (sf_s) in the induction machine. The variation of the measured rotor resistance versus $i_{\rm ds}$ at different excitation frequencies obtained using the blocked rotor test is presented in Fig. 22. Note that since the current is only applied on d-axis ($i_{\rm qs} = 0$) in this test, there is no torque production and rotor does not rotate, hence, there is no need to block the rotor. It can be observed from Fig. 22 that the estimated rotor resistance is independent of the stator d-axis current, however, changing excitation frequency affects the rotor resistance estimation due to the ac effects (skin effect because of the large cross-section of rotor bars). Assuming a slip frequency of 20 Hz (rated frequency of the test IM is 166.7 Hz at the rated speed of 5000 rpm), the rotor resistance is estimated to be around $R_r = 1.45$ mΩ.

Rotor resistance can also vary with temperature, however, it is not possible to measure the rotor temperature in the test setup. The calculated reference points using the proposed control algorithm are not dependent on rotor resistance variation because there is no rotor resistance term in the equations used to calculate the reference points. However, because slip estimation is dependent on rotor resistance in (27), any parameter mismatch can lead to incorrect slip estimation which may affect the performance of the controller. The rotor resistance is measured using the blocked rotor test at 25 °C. Assuming the maximum

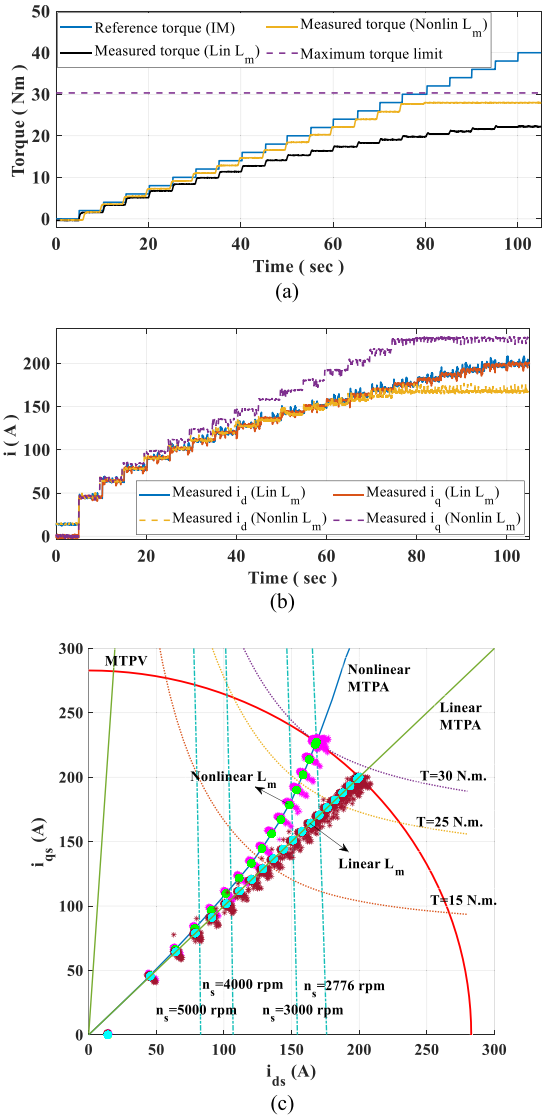

Fig. 24. Experimental results with reference torque steps at 500 rpm with and without considering magnetic saturation. (a) Torque. (b) Current. (c) Operating points trajectory.

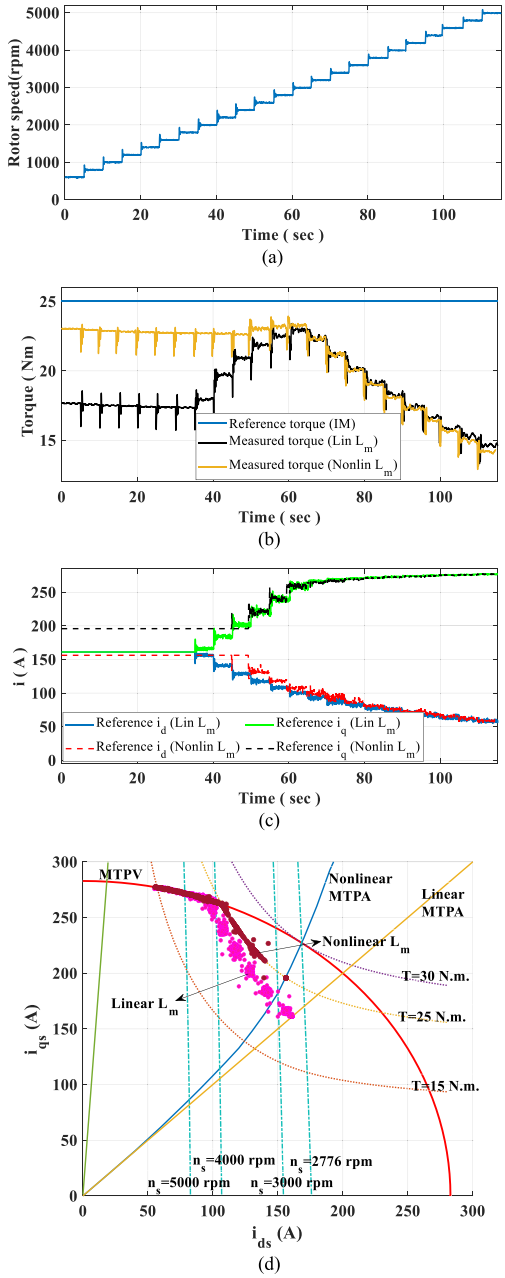

Fig. 25. Experimental results with speed steps and reference torque of 25 Nm with and without considering magnetic saturation. (a) Mechanical speed. (b) Torque. (c) Current. (d) Operating points trajectory.

rotor temperature of 90 °C, the rotor temperature can rise up to 1.82 mΩ. In order to investigate the effect of rotor resistance variation on the performance of the controller, reference speed steps (600–5000 rpm with 200 rpm steps) are applied under load torque of 15 Nm. The test is repeated for three different rotor resistance values ($R_r = 1.45$ mΩ, 1.6 mΩ, and 1.82 mΩ). The experimental results for three different rotor resistance values are presented in Fig. 23. Based on Fig. 23(c), it can be seen that the calculation of reference points is not affected by rotor resistance variation. The measured torque is the same for three rotor resistance values at lower speeds. However, as speed increases the measured torque is reduced when R_r is not well predicted. This is because of incorrect slip estimation and hence incorrect estimation of the synchronous speed. In other words, the rotor field is not completely aligned with d-axis in case of the parameter mismatch. Based on Fig. 23(b), the maximum torque error happens at 5000 rpm (maximum speed of IM) where the measured torque with $R_r = 1.82$ mΩ (11.31 Nm) is about 15% less than the measured torque with $R_r = 1.45$ mΩ (13.41 Nm). Hence, in the worst-case scenario, the rotor resistance mismatch can result in the torque error of maximum 15%.

E. Comparison to the Literature

In most of the proposed methods in the literature, the core saturation effect has been neglected and magnetizing inductance (L_m) is assumed to be constant. In order to show the effectiveness of considering the variation of the magnetizing inductance,

experimental test results with and without considering the magnetic saturation effect are provided and compared in this section.

The experimental results in the MTPA region at 500 rpm while reference torque steps are applied are presented in Fig. 24. It can be observed from Fig. 24(b) that both *d* and *q* axes currents are equal (which is the linear MTPA condition) at each operating point when the saturation effect is neglected. The torque error is significantly bigger when the saturation effect is neglected as shown in Fig. 24(a). The operating point trajectory for reference and measured currents are presented in Fig. 24(c). It can be observed that the operating points are on the linear and the proposed nonlinear MTPA curves.

In order to investigate the effectiveness of considering the saturation effect in the field-weakening region, the speed steps (600–5000 rpm with the steps of 200 rpm) are applied under constant reference torque of 25 Nm. The experimental results are presented in Fig. 25. It can be seen that the difference between the measured torques with and without considering the saturation effect is significant when IM operates on the MTPA curve ($t =$ 0–35 s). By increasing the speed, $i_{\rm ds}$ is reduced and IM operates in the field-weakening region. As $i_{\rm ds}$ is reduced, the difference between the linear (nominal) and nonlinear L_m and hence, the difference between the measured torques with and without considering saturation effect decreases. Variation of reference *d* and *q* axes currents for both the cases are shown in Fig. 25(c). The difference between the operating point trajectories for the reference currents with and without considering saturation are shown in Fig. 25(d). It can be observed that the difference decreases as the *d*-axis current is reduced in the field-weakening region.

VI. Conclusion

An online optimization-based optimal tracking control algorithm is proposed in this article to control IM drives in MTPA, field-weakening, and MTPV regions. The optimization problems are formulated and solved using the Lagrange multipliers method to obtain analytical MTPA and MTPV conditions considering the core saturation effect which is usually ignored in the existing literature. Moreover, stator resistive drop terms, inverter nonlinear voltage drop, and dc-link voltage variations are considered in generating the optimal reference points. A simple and straightforward method is proposed by dividing the entire operating region of IM into four regions. The reference points are then generated once the corresponding region is detected. Smooth operation of the proposed controller between MTPA and field-weakening regions is verified using simulations. All nonlinear equations are solved online using the golden section method. The effectiveness of the proposed online optimal tracking control method in controlling IM over the entire speed and torque ranges is verified with experimental results on a 4.7 kW, 4-pole, three-phase IM drive.

Acknowledgment

This article is dedicated to the memory of Iman Aghabali and Mehdi Eshaghian.

References

[1] A. M. Bazzi and P. T. Krein, "Review of methods for real-time loss minimization in induction machines," *IEEE Trans. Ind. Appl.*, vol. 46, no. 6, pp. 2319–2328, Nov./Dec. 2010.

[2] H. A. Zarchi, H. M. Hesar, and M. A. Khoshhava, "Online maximum torque per power losses strategy for indirect rotor flux-oriented control-based induction motor drives," *IET Electr. Power Appl.*, vol. 13, no. 2, pp. 259–265, Feb. 2018.

[3] S. A. Odhano, R. Bojoi, A. Boglietti, Ş. G. Roşu, and G. Griva, "Maximum efficiency per torque direct flux vector control of induction motor drives," *IEEE Trans. Ind. Appl.*, vol. 51, no. 6, pp. 4415–4424, Nov./Dec. 2015.

[4] S. Bozhko, S. Dymko, S. Kovbasa, and S. M. Peresada, "Maximum torque-per-amp control for traction IM drives: Theory and experimental results," *IEEE Trans. Ind. Appl.*, vol. 53, no. 1, pp. 181–193, Jan./Feb. 2017.

[5] A. Borisevich and G. Schullerus, "Energy efficient control of an induction machine under torque step changes," *IEEE Trans. Energy Convers.*, vol. 31, no. 4, pp. 1295–1303, Dec. 2016.

[6] D. Casadei, M. Mengoni, G. Serra, A. Tani, and L. Zarri, "A control scheme with energy saving and DC-link overvoltage rejection for induction motor drives of electric vehicles," *IEEE Trans. Ind. Appl.*, vol. 46, no. 4, pp. 1436–1446, Jul./Aug. 2010.

[7] D. S. Kirschen, D. W. Novotny, and T. A. Lipo, "On-line efficiency optimization of a variable frequency induction motor drive," *IEEE Trans. Ind. Appl.*, vol. IA-21, no. 3, pp. 610–616, May 1985.

[8] S. Sridharan and P. T. Krein, "Minimization of system-level losses in VSI-based induction motor drives: offline strategies," *IEEE Trans. Ind. Appl.*, vol. 53, no. 2, pp. 1096–1105, Mar./Apr. 2017.

[9] A. A. C. Rebolledo and M. A. Valenzuela, "Expected savings using loss-minimizing flux on IM drives—Part I: Optimum flux and power savings for minimum losses," *IEEE Trans. Ind. Appl.*, vol. 51, no. 2, pp. 1408–1416, Mar./Apr. 2015.

[10] R. H. Kumar, A. Iqbal, and N. C. Lenin, "Review of recent advancements of direct torque control in induction motor drives—A decade of progress," *IET Power Electron.*, vol. 11, no. 1, pp. 1–15, Jan. 2018.

[11] I. M. Alsofyani, N. R. N. Idris, and K.-B. Lee, "Dynamic hysteresis torque band for improving the performance of lookup-table-based DTC of induction machines," *IEEE Trans. Power Electron.*, vol. 33, no. 9, pp. 7959–7970, Sep. 2018.

[12] A. Berzoy, J. Rengifo, and O. Mohammed, "Fuzzy predictive DTC of Induction machines with reduced torque ripple and high-performance operation," *IEEE Trans. Power Electron.*, vol. 33, no. 3, pp. 2580–2587, Mar. 2018.

[13] Z. Wang, K. Zhang, and J. Kan, "Indirect vector control with simplified rotor resistance adaptation for induction machines," *IET Power Electron.*, vol. 8, no. 7, pp. 1284–1294, Jul. 2015.

[14] L. Liu, X. Du, and S. Shen, "Indirect field-oriented torque control of induction motor considering magnetic saturation effect: Error analysis," *IET Elect. Power Appl.*, vol. 11, no. 6, pp. 1105–1113, Jul. 2017.

[15] Y. Zhang, Y. Bai, H. Yang, and B. Zhang, "Low switching frequency model predictive control of three-level inverter-fed IM drives with speed-sensorless and field-weakening operations," *IEEE Trans. Ind. Electron.*, vol. 66, no. 6, pp. 4262–4272, Jun. 2019.

[16] A. Bhowate, M. Aware, and S. Sharma, "Predictive torque control with online weighting factor computation technique to improve performance of induction motor drive in low speed region," *IEEE Access*, vol. 7, pp. 42309–42321, 2019.

[17] Sun Jin, Zheng Wei, and Hou Zhenyi, "One novel scalar control scheme for induction machine," in *Proc. 30th Annu. Conf. IEEE Ind. Electron. Soc.*, vol. 1, 2004, pp. 347–352.

[18] S. Gadoue, M. Armstrong, A. Smith, and J. Finch, "Improved method for the scalar control of induction motor drives," *IET Elect. Power Appl.*, vol. 7, no. 6, pp. 487–498, Jul. 2013.

[19] A. Munoz-Garcia, T. A. Lipo, and D. W. Novotny, "A new induction motor V/f control method capable of high-performance regulation at low speeds," *IEEE Trans. Ind. Appl.*, vol. 34, no. 4, pp. 813–821, Jul./Aug. 1998.

[20] M. H. Park and S. K. Sul, "Microprocessor-based optimal-efficiency drive of an induction motor," *IEEE Trans. Ind. Electron.*, vol. IE-31, no. 1, pp. 69–73, Feb. 1984.

[21] Y. Zhang, B. Zhang, H. Yang, M. Norambuena, and J. Rodriguez, "Generalized sequential model predictive control of IM drives with field-weakening ability," *IEEE Trans. Power Electron.*, vol. 34, no. 9, pp. 8944–8955, Sep. 2019.

[22] X. Yang and X. Zheng, "Gradient descent algorithm-based adaptive NN control design for an induction motor," *IEEE Trans. Syst. Man, Cybern. Syst.*, to be published.

[23] X. Fu and S. Li, "A novel neural network vector control technique for induction motor drive," *IEEE Trans. Energy Convers.*, vol. 30, no. 4, pp. 1428–1437, Dec. 2015.
[24] J.-F. Stumper, A. Dötlinger, and R. Kennel, "Loss minimization of induction machines in dynamic operation," *IEEE Trans. Energy Convers.*, vol. 28, no. 3, pp. 726–735, Sep. 2013.
[25] Z. Qu, M. Ranta, M. Hinkkanen, and J. Luomi, "Loss-minimizing flux level control of induction motor drives," *IEEE Trans. Ind. Appl.*, vol. 48, no. 3, pp. 952–961, May/Jun. 2012.
[26] W. Sung, J. Shin, and Y. Jeong, "Energy-efficient and robust control for high-performance induction motor drive with an application in electric vehicles," *IEEE Trans. Veh. Technol.*, vol. 61, no. 8, pp. 3394–3405, Oct. 2012.
[27] M. N. Uddin and S. W. Nam, "New online loss-minimization-based control of an induction motor drive," *IEEE Trans. Power Electron.*, vol. 23, no. 2, pp. 926–933, Mar. 2008.
[28] M. N. Uddin and S. W. Nam, "Development of a nonlinear and model-based online loss minimization control of an IM drive," *IEEE Trans. Energy Convers.*, vol. 23, no. 4, pp. 1015–1024, Dec. 2008.
[29] G. Dong and O. Ojo, "Efficiency optimizing control of induction motor using natural variables," *IEEE Trans. Ind. Electron.*, vol. 53, no. 6, pp. 1791–1798, Dec. 2006.
[30] P. Famouri and J. J. Cathey, "Loss minimization control of an induction motor drive," *IEEE Trans. Ind. Appl.*, vol. 27, no. 1, pp. 32–37, Jan./Feb. 1991.
[31] I. Kioskeridis and N. Margaris, "Loss minimization in induction motor adjustable-speed drives," *IEEE Trans. Ind. Electron.*, vol. 43, no. 1, pp. 226–231, Feb. 1996.
[32] H. Grotstollen and J. Wiesing, "Torque capability and control of a saturated induction motor over a wide range of flux weakening," *IEEE Trans. Ind. Electron.*, vol. 42, no. 4, pp. 374–381, Aug. 1995.
[33] S.-H. Kim and S.-K. Sul, "Maximum torque control of an induction machine in the field weakening region," *IEEE Trans. Ind. Appl.*, vol. 31, no. 4, pp. 787–794, Jul./Aug. 1995.
[34] M. Mengoni, L. Zarri, A. Tani, G. Serra, and D. Casadei, "A comparison of four robust control schemes for field-weakening operation of induction motors," *IEEE Trans. Power Electron.*, vol. 27, no. 1, pp. 307–320, Jan. 2012.
[35] B. Wang, X. Zhang, Y. Yu, J. Zhang, and D. Xu, "Maximum torque analysis and extension in six-step mode-combined field-weakening control for induction motor drives," *IEEE Trans. Ind. Electron.*, vol. 66, no. 12, pp. 9129–9138, Dec. 2019.
[36] S.-H. Kim and S.-K. Sul, "Voltage control strategy for maximum torque operation of an induction machine in the field-weakening region," *IEEE Trans. Ind. Electron.*, vol. 44, no. 4, pp. 512–518, Aug. 1997.
[37] B. J. Seibel, T. M. Rowan, and R. J. Kerkman, "Field-oriented control of an induction machine in the field-weakening region with DC-link and load disturbance rejection," *IEEE Trans. Ind. Appl.*, vol. 33, no. 6, pp. 1578–1584, Nov./Dec. 1997.
[38] X. Xu and D. W. Novotny, "Selection of the flux reference for induction machine drives in the field weakening region," *IEEE Trans. Ind. Appl.*, vol. 28, no. 6, pp. 1353–1358, Nov./Dec. 1992.
[39] Z. Dong, Y. Yu, W. Li, B. Wang, and D. Xu, "Flux-weakening control for induction motor in voltage extension region: Torque analysis and dynamic performance improvement," *IEEE Trans. Ind. Electron.*, vol. 65, no. 5, pp. 3740–3751, May 2018.
[40] Z. Dong *et al.*, "Operating point selected flux-weakening control of induction motor for torque-improved high-speed operation under multiple working conditions," *IEEE Trans. Power Electron.*, vol. 34, no. 12, pp. 12011–12023, Dec. 2019.
[41] S. K. Sahoo and T. Bhattacharya, "Field weakening strategy for a vector-controlled induction motor drive near the six-step mode of operation," *IEEE Trans. Power Electron.*, vol. 31, no. 4, pp. 3043–3051, Apr. 2016.
[42] J.-K. Seok and S. Kim, "Hexagon voltage manipulating control (HVMC) for AC motor drives operating at voltage limit," *IEEE Trans. Ind. Appl.*, vol. 51, no. 5, pp. 3829–3837, Sep./Oct. 2015.
[43] Y. Liu, J. Zhao, R. Wang, and C. Huang, "Performance improvement of induction motor current controllers in field-weakening region for electric vehicles," *IEEE Trans. Power Electron.*, vol. 28, no. 5, pp. 2468–2482, May 2013.
[44] P.-Y. Lin and Y.-S. Lai, "Novel voltage trajectory control for field-weakening operation of induction motor drives," *IEEE Trans. Ind. Appl.*, vol. 47, no. 1, pp. 122–127, Jan./Feb. 2011.
[45] M. Mengoni, L. Zarri, A. Tani, G. Serra, and D. Casadei, "Stator flux vector control of induction motor drive in the field weakening region," *IEEE Trans. Power Electron.*, vol. 23, no. 2, pp. 941–949, Mar. 2008.
[46] G. Gallegos-Lopez, F. S. Gunawan, and J. E. Walters, "Current control of induction machines in the field-weakened region," *IEEE Trans. Ind. Appl.*, vol. 43, no. 4, pp. 981–989, Jul./Aug. 2007.
[47] R. Tarvirdilu-Asl, S. Nalakath, Y. Sun, J. Wiseman, and A. Emadi, "Optimal control of induction motor in field weakening region considering inverter nonlinearity," in *Proc. IEEE Transp. Electrif. Conf. Expo.*, 2019, pp. 1–8.
[48] G. Pellegrino, R. I. Bojoi, P. Guglielmi, and F. Cupertino, "Accurate inverter error compensation and related self-commissioning scheme in sensorless induction motor drives," *IEEE Trans. Ind. Appl.*, vol. 46, no. 5, pp. 1970–1978, Sep./Oct. 2010.
[49] D. E. Salt, D. Drury, D. Holliday, A. Griffo, P. Sangha, and A. Dinu, "Compensation of inverter nonlinear distortion effects for signal-injection-based sensorless control," *IEEE Trans. Ind. Appl.*, vol. 47, no. 5, pp. 2084–2092, Sep./Oct. 2011.
[50] L. Tang and M. F. Rahman, "A direct torque controlled interior permanent magnet synchronous machine drive with compensation of the forward voltage drops of the power switches," in *Proc. 38th IAS Annu. Meeting Conf. Rec. Ind. Appl. Conf.*, vol. 1, 2003, pp. 625–631.
[51] Z. Xia, S. Nalakath, R. Tarvirdilu-Asl, Y. Sun, J. Wiseman, and A. Emadi, "Online optimal tracking method for interior permanent magnet machines with improved MTPA and MTPV in whole speed and torque ranges," *IEEE Trans. Power Electron.*, to be published.
[52] L. Zhao, J. Huang, H. Liu, B. Li, and W. Kong, "Second-order sliding-mode observer with online parameter identification for sensorless induction motor drives," *IEEE Trans. Ind. Electron.*, vol. 61, no. 10, pp. 5280–5289, Oct. 2014.
[53] H. Wang, X. Ge, and Y.-C. Liu, "Second-order sliding-mode MRAS observer-based sensorless vector control of linear induction motor drives for medium-low speed Maglev applications," *IEEE Trans. Ind. Electron.*, vol. 65, no. 12, pp. 9938–9952, Dec. 2018.
[54] M. S. Zaky, M. M. Khater, S. S. Shokralla, and H. A. Yasin, "Wide-speed-range estimation with online parameter identification schemes of sensorless induction motor drives," *IEEE Trans. Ind. Electron.*, vol. 56, no. 5, pp. 1699–1707, May 2008.

Rasul Tarvirdilu-Asl (Student Member, IEEE) received the B.Sc. degree from the Amirkabir University of Technology, Tehran, Iran, in 2013, and the M.Sc. degree from Middle East Technical University, Ankara, Turkey, in 2016, both in electrical engineering. He is currently working toward the Ph.D. degree in electrical engineering at McMaster University, Hamilton, ON, Canada.

In 2017, he joined McMaster Automotive Resource Center. His research interests include design, modeling, and control of electric motor drives and power electronics.

Shamsuddeen Nalakath (Senior Member, IEEE) received the M.S. degree in electrical engineering from Indian Institute of Technology, Madras, India, in 2010, and the Ph.D. degree in electrical engineering from McMaster University, Hamilton, ON, Canada, in 2018.

He is currently a Senior Principle Engineer with Enedym Inc., Hamilton, ON, Canada, responsible for design and development of electric motor inverters and controls. From 2018 to 2019, he was a Principal Research Engineer with McMaster Automotive Resource Center, McMaster University, Hamilton, ON, Canada, where he led industrial research projects on electric motor controls and inverters for automotive applications. From 2010 to 2014, he was with the Advanced Engineering Group, M/s TVS Motor Company Ltd., India, where he worked in design and development of advanced electric machines for electric and hybrid vehicles. His research interests include electric motor control, electric motor design, and power electronics for high-performance automotive traction applications.

Zekun Xia (Student Member, IEEE) received the B.S. and M.S. degrees in electrical engineering from the Northwestern Polytechnical University, Xi'an, China, in 2014 and 2017, respectively. He is currently working toward the Ph.D. degree in electrical engineering with McMaster Automotive Resource Centre, McMaster University, Hamilton, ON, Canada.

His research interests include electric machines and drives with emphasis on optimal control for permanent magnet machines, switched reluctance machines, and induction machines.

Yingguang Sun (Member, IEEE) received the M.S. degree in electrical engineering from the Illinois Institute of Technology (IIT), Chicago, IL, USA, in 2013, and the Ph.D. degree from McMaster University, Hamilton, ON, Canada, in 2016.

He is currently working as a Motor Control Engineer with BorgWarner Waterloo Inc. (previously known as Sevcon Canada). In 2017, he was a Motor Control Firmware Engineer with Rockwell Automation in Canada. From 2013 to 2016, he was a Research Assistant with the Canada Excellence Research Chair in Hybrid Powertrain Program, Hamilton, ON, Canada. From September 2012 to June 2013, he served as a Research Assistant with Electric Drives and Energy Conversion Laboratory, IIT, Chicago, IL, USA. His research interests include advanced high-performance control methods for electric motor drives and power electronics applications in electrified transportation systems.

Dr. Sun was the recipient of the best presentation prize in IECON 2015, Yokohama, Japan.

Jason Wiseman received the B.Eng. degree from Ryerson University, Toronto, ON, Canada, in 1997, and the M.E.Sc. degree from the University of Western Ontario, London, ON, Canada, in 2001.

He is currently working as an Engineering Manager with BorgWarner Waterloo Inc. (previously known as Sevcon Canada). From 2009 to 2015, he worked as a Motor Control Firmware Engineer with Accelerated Systems Inc., a Digital Controls Engineer at Satcon Technology Corp from 2007 to 2009, and a Motor Control Firmware Engineer at Rockwell Automation from 1999 to 2007 in Canada.

His research interests include control of inverter and converters for motor control and renewable energy applications.

Ali Emadi (Fellow, IEEE) received the B.S. and M.S. degrees in electrical engineering with highest distinction from the Sharif University of Technology, Tehran, Iran, in 1995 and 1997, respectively, and the Ph.D. degree in electrical engineering from Texas A&M University, College Station, TX, USA, in 2000.

He is the Canada Excellence Research Chair Laureate with McMaster University, Hamilton, ON, Canada. He is also the holder of the NSERC/FCA Industrial Research Chair with the Electrified Powertrains and Tier I Canada Research Chair with the Transportation Electrification and Smart Mobility. Before joining McMaster University, he was the Harris Perlstein Endowed Chair Professor of Engineering and Director of the Electric Power and Power Electronics Center and Grainger Laboratories, Illinois Institute of Technology, Chicago, IL, USA, where he established research and teaching facilities as well as courses in power electronics, motor drives, and vehicular power systems. He was the Founder, Chairman, and President of Hybrid Electric Vehicle Technologies, Inc.—a university spin-off company of Illinois Tech. He has authored/coauthored more than 450 journals and conference papers as well as several books including *Vehicular Electric Power Systems* (2003), *Energy Efficient Electric Motors* (2004), *Uninterruptible Power Supplies and Active Filters* (2004), *Modern Electric, Hybrid Electric, and Fuel Cell Vehicles* (2nd ed, 2009), *and Integrated Power Electronic Converters and Digital Control* (2009). He is also the editor of the *Handbook of Automotive Power Electronics and Motor Drives* (2005) *and Advanced Electric Drive Vehicles* (2014). He is the co-editor of the *Switched Reluctance Motor Drives* (2018).

Dr. Emadi has been the recipient of numerous awards and recognitions. He was the Advisor for the Formula Hybrid Teams at Illinois Tech and McMaster University, which won the GM Best Engineered Hybrid System Award at the 2010, 2013, and 2015 competitions. He was the Inaugural General Chair of the 2012 IEEE Transportation Electrification Conference and Expo and has chaired several IEEE and SAE conferences in the areas of vehicle power and propulsion. He is the founding Editor-in-Chief of the IEEE TRANSACTIONS ON TRANSPORTATION ELECTRIFICATION.